

1 **GUST1.0: A GPU-accelerated 3D Urban Surface Temperature Model**

2 Shuo-Jun Mei^{1,2*}, Guanwen Chen^{1,2}, Jian Hang^{1,2}, Ting Sun³

3 ¹ School of Atmospheric Sciences, Sun Yat-sen University, and Southern Marine Science and
4 Engineering Guangdong Laboratory (Zhuhai), Zhuhai 519082, PR China

5 ² China Meteorological Administration Xiong'an Atmospheric Boundary Layer Key Laboratory,
6 Xiong'an, P.R. China

7 ³ Department of Risk and Disaster Reduction, University College London, London, UK

8 *Correspondence to:* Shuo-Jun Mei (meishj@mail.sysu.edu.cn)

9 **Abstract**

10 The escalating urban heat, driven by climate change and urbanization, poses significant threats to
11 residents' health and urban climate resilience. The coupled radiative-convective-conductive heat transfer
12 across complex urban geometries makes it challenging to identify the primary causes of urban heat and
13 develop mitigation strategies. To address this challenge, we develop a GPU-accelerated Urban Surface
14 Temperature model (GUST) through CUDA architecture. To simulate the complex radiative exchanges
15 and coupled heat transfer processes, we adopt Monte Carlo method, leveraging GPUs to overcome its
16 computational intensity while retaining its high accuracy. Radiative exchanges are resolved using a
17 reverse ray tracing algorithm, while the conduction-radiation-convection mechanism is addressed
18 through a random walking algorithm. The validation is carried out using the Scaled Outdoor
19 Measurement of Urban Climate and Health (SOMUCH) experiment, which features a wide range of
20 urban densities and offers high spatial and temporal resolution. This model exhibits notable accuracy in
21 simulating urban surface temperatures and their temporal variations across different building densities.
22 Analysis of the surface energy balance reveals that longwave radiative exchanges between urban surfaces
23 significantly influence model accuracy, whereas convective heat transfer has a lesser impact. To
24 demonstrate the applicability of GUST, it is employed to model transient surface temperature
25 distributions at complex geometries on a neighborhood scale. Leveraging the high computational
26 efficiency of GPU, the simulation traces 10^5 rays across 2.3×10^4 surface elements in each time step,
27 ensuring both accuracy and high-resolution results for urban surface temperature modeling.

28 **1. Introduction**

29 Urban overheating has become a pressing issue due to the combination effects of global warming,
30 heatwaves, and rapid urbanization ([Feng et al., 2023](#)). The Urban Heat Island (UHI) effect is
31 characterized by higher surface and air temperatures in urban areas than in surrounding rural areas, which
32 exacerbates the urban overheating ([Manoli et al., 2019](#)). It is estimated that more than 1.7 billion people
33 and 13,000 cities are facing urban overheating problems ([Tuholske et al., 2021](#)). Exposure to extreme
34 urban heat poses a significant threat to residents' health, contributing to increased mortality and morbidity
35 ([Ebi et al., 2021](#)).

36 To tackle urban overheating, a precise understanding of the factors driving excessive surface heat is
37 essential, making accurate modeling of urban surface temperatures a critical step toward developing
38 effective mitigation strategies. Urban surface temperatures are commonly simulated with urban land
39 surface schemes (LSMs). To capture the complex exchanges of energy and momentum within an urban
40 environment, these schemes range from simplified approaches that represent the city as a single
41 impervious slab to advanced frameworks that explicitly incorporate the three-dimensional geometry of
42 buildings with varying heights and material properties. The Urban-PLUMBER project has evaluated 32
43 such schemes ([Grimmond et al., 2010](#); [Grimmond et al., 2011](#)), and classified them into ten categories
44 based on the level of three-dimensional detail represented. The most detailed of these are the building-
45 resolved schemes, which explicitly solve airflow and heat transfer while representing the full three-
46 dimensional urban landscape.

47 Building-resolved models, such as VTUF ([Nice, 2016](#)) and computational fluid dynamics (CFD) tools
48 ([Carmeliet and Derome, 2024](#)), solve the governing physical processes at high spatial and temporal
49 resolution. These models are powerful tools for examining the urban thermal balance and identifying the
50 primary drivers of urban heat ([Carmeliet and Derome, 2024](#)). They enable a quantitative evaluation of
51 the contribution of each process, such as conduction, radiation, and convection, to the overall thermal
52 balance. This is particularly important for Asia cities, which are characterized by high-density, high-rise
53 developments and complex urban geometry. Findings from the Scaled Outdoor Measurement of Urban
54 Climate and Health (SOMUCH) project highlight the intricate influence of building morphology on the

55 thermal environment, especially under super-high-density conditions ([Hang and Chen, 2022](#)). These
56 effects arise from complex three-dimensional urban landscapes, including irregular building forms and
57 intricate shading patterns. Accordingly, models representing high-density Asian cities need greater
58 accuracy and flexibility to account for these features.

59 Building-resolved urban surface temperatures are determined by the coupled heat transfer processes of
60 conduction, radiation, and convection ([Krayenhoff and Voogt, 2007](#)). These heat transfer processes in
61 urban areas differ from those in rural areas. First, urban materials typically have a lower heat capacity,
62 allowing them to heat up more quickly and reach higher temperatures ([Wang et al., 2018](#)). Secondly, the
63 complex three-dimensional geometry of urban environments leads to multiple reflections, which reduce
64 reflected solar radiation and limit the longwave heat loss to sky ([Yang and Li, 2015](#)). Thirdly, the densely
65 packed buildings weaken the urban wind and thus reduce the convective transfer and further limit the
66 heat loss ([Wang et al., 2021](#)).

67 A well-designed building-resolved model needs to accurately capture these heat transfer processes. Table
68 1 summarizes the models for urban surface temperatures and their schemes for conduction, radiation,
69 and convection. For heat conduction, 1D models are commonly used due to the relatively thin walls of
70 buildings in urban areas. For convective heat transfer, both parameterized convective coefficients and
71 CFD simulations are commonly used. CFD simulations can better capture the spatial variations in air
72 temperature in densely built urban areas, but the computational cost is much higher.

73 The key distinction among these models lies in their radiation schemes, as radiation is the primary energy
74 input into the thermal system of urban surfaces. Moreover, simulating complex urban radiative transfer
75 requires significant computational resources, necessitating simplifications and parameterizations to make
76 the simulation more applicable. For the radiative exchange between urban surfaces, the radiosity method
77 is widely adopted. This approach first collects luminous energy from direct solar and diffuse sky sources
78 and then redistributes reflected energy according to view factors, which quantify the geometric
79 relationships among surfaces. View factors can be determined analytically for simple geometries,
80 estimated with the discrete transfer method (hemisphere discretization and ray counting), or calculated
81 using Monte Carlo ray tracing (MCRT). However, the radiosity method assumes purely diffuse

82 reflections and depends on precise view-factor calculations, making it less accurate for complex urban
83 geometries and surfaces containing semi-transparent materials.

84 In contrast, the MCRT approach offers greater flexibility and has been widely employed to model solar
85 radiation on complex urban surfaces ([Kondo et al., 2001](#)). More recently, its use has expanded beyond
86 radiative transfer to encompass coupled conduction, convection, and radiation processes ([Villefranque et](#)
87 [al., 2022](#)). In backward MCRT, the energy of the incident light is divided into a large number of photons.
88 By tracking the path of these photons and counting the number of photons absorbed, the net solar
89 radiation reaching a given surface can be calculated. For example, the HTRDR-Urban adopted the
90 backward MCRT, to calculate the solar radiation considering multiple reflections ([Schoetter et al., 2023](#)).
91 Building on this concept, [Tregan et al. \(2023\)](#) proposed a theoretical framework to solve linearized
92 transient conduction-radiation problems with Robin's boundary condition in complex 3D urban geometry.
93 Based on that framework, [Caliot et al. \(2024\)](#) developed a probabilistic model to simulate urban surface
94 temperatures, using ray-tracing, walk-on-sphere and double randomization techniques. Their model
95 leverages advancements in computer graphics for image synthesis and the MCM, enabling it to
96 effectively handle large and complex 3D geometries.

97 The MCRT method has demonstrated strong capability for accurately modeling coupled heat and
98 radiation processes in complex urban environments, but its high computational cost and low efficiency
99 currently limit its application to real-world urban configurations. Although several models listed in Table
100 1 have been validated against field measurements, others remain unverified and rely on various
101 assumptions and parameterizations, which reduces confidence in their accuracy. Furthermore, the use of
102 field measurement data for model validation faces persistent challenges: 1) limited test points due to
103 regulatory constraints and installation difficulties, 2) uncertainty in infrared imagery caused by varying
104 view angles, and 3) heterogeneity in the optical and thermal properties of building materials.

105 This study aims to develop a GPU-accelerated Urban Surface Temperature (GUST) model to enhance
106 the computational speed of Monte Carlo Method. The model is designed to operate at the neighborhood
107 scale and to capture microscale processes, including complex shading patterns, multiple reflections of
108 solar radiation, and longwave radiative exchanges between building surfaces and the ground. The

109 ultimate objective is to identify the physical drivers of extreme heat in high-density urban neighborhoods.
110 The absorption and reflection of longwave and solar radiation on outdoor surfaces modeled using the
111 reverse Monte Carlo ray tracing (rMCRT) algorithm. The resulting solar and longwave radiation are then
112 treated as heat flux boundary conditions for the 1D heat conduction model, which employs the Monte
113 Carlo random walk method to calculate surface temperatures. High spatial-temporal resolution surface
114 temperature data from a scaled measurement (SOMUCH) is employed to validate the parameterization
115 and assumptions in this model.

116 The paper is organized as follows. Sect. 2 outlines the model structure and describes the algorithms used
117 for the submodels. Sect. 3 presents the validation and evaluation of the model by comparing it with
118 experimental data. Sect. 4 includes an example demonstrating how the model can be applied to complex
119 geometries. Sect. 5 discusses the applications, limitations, and future development of the model. Lastly,
120 Sect. 6 provides the conclusions.

121

122 **Table 1.** Overview of building-resolved models for urban surface temperature. The view factors are
123 solved by both DTM (Discrete transfer method), analytical model, and Monte Carlo ray tracing method.

| Model | Solar Irradiation | Reflections and Conduction longwave exchange | Convection | Validation |
|---|----------------------------------|---|-----------------------------|---|
| HTRDR-Urban (Schoetter et al., 2023) | Backward Monte Carlo ray tracing | Backward Monte Carlo ray tracing | Monte Carlo random walking | Parameterized N.A. |
| MUST (Yang and Li, 2013) | Sunlit-shaded distributions | Radiosity Method, DTM view factors | 1D heat conduction | Parameterized Thermal scanner and IRT (Voogt and Oke, 1998) |
| TUF-3D (Krayenhoff and Voogt, 2007) | Sunlit-shaded distributions | Radiosity Method, analytical view factors | 1D heat conduction | Parameterized Thermal scanner and IRT (Voogt and Oke, 1998) |
| SOLENE Microclimat (Imbert et al., 2018) | Sunlit-shaded distributions. | Radiosity Method, analytical view factors | 1D heat conduction | Coupling CFD simulation Thermographies measurement (Hénon et al., 2012) |
| Envi-Met (Eingrüber et al., 2024) | Flux reduction coefficients | Radiosity Method, DTM view factors | 1D heat conduction | Coupling CFD simulation Field measurements (Forouzandeh, 2021) |
| uDALES (Owens et al., 2024) | Sunlit-shaded distributions | Radiosity Method, DTM view factors | 1D heat conduction | Coupling CFD simulation N.A. |
| PALM (Resler et al., 2017) | Sunlit-shaded distributions | Radiosity Method, Analytical and DTM view factors | Empirical heat conductivity | Coupling CFD simulation Field measurement (Resler et al., 2017) |
| MITRAS (Salim et al., 2018) | Meso-scale radiation scheme | Meso-scale radiation scheme (METRAS) | Force-restore method | Coupling CFD simulation N.A. |
| OpenFOAM (Rodriguez et al., 2024) | Sunlit-shaded distributions | Radiosity Method, DTM view factor | 1D heat-moisture diffusion. | Coupling CFD simulation N.A. |
| FLUENT (Toparlar et al., 2015) | Sunlit-shaded distributions | Radiosity Method, DTM view factor | Shell conduction | Coupling CFD simulation Field measurement (Toparlar et al., 2015) |

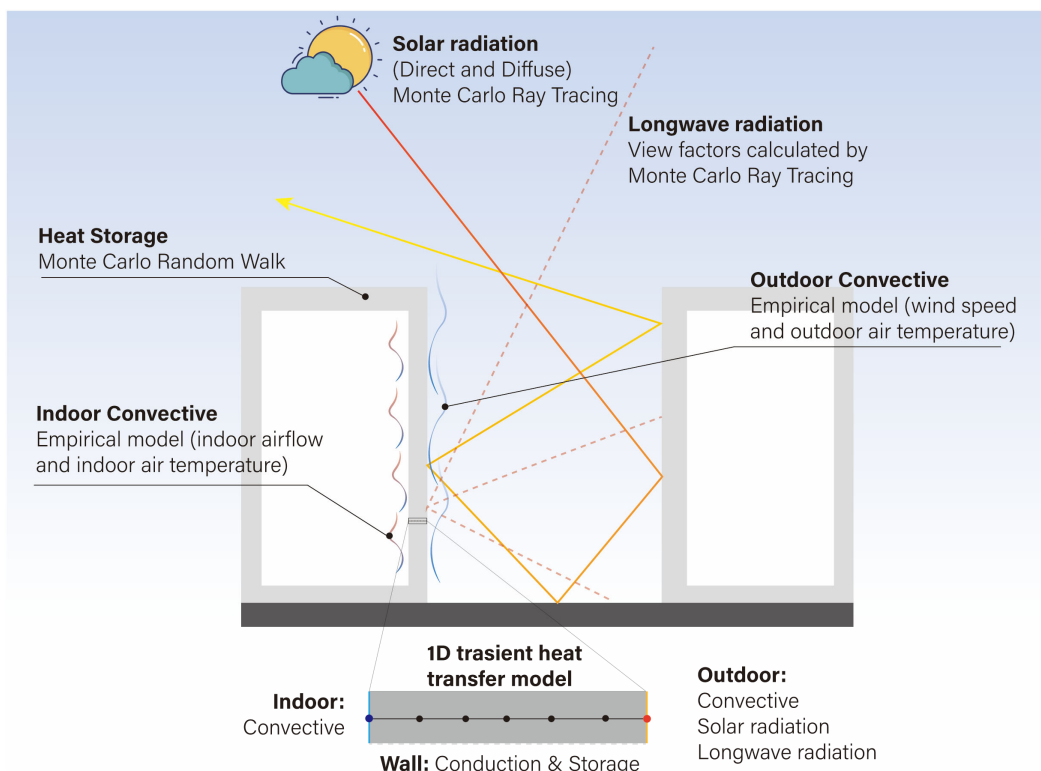
124

125 **2. Model design**

126 GUST aims to resolve the urban surface temperature by a transient heat conduction model, as illustrated
 127 in Fig. 1. The convective and radiative heat transfer at urban surfaces is treated as boundary conditions
 128 for the 1D heat conduction model. For the outdoor side, the heat flux (q_{out}) is the sum of radiative
 129 (longwave q_l and solar q_s) and convective heat flux ($q_{c,out}$).

130
$$q_{out} = q_l + q_s + q_{c,out} \quad (1)$$

131 The absorbed solar radiation, q_s is the sum of direct solar irradiation ($q_{s,o}$) and diffuse solar irradiation
 132 ($q_{s,r}$), expressed by: $q_s = q_{s,o} + q_{s,r}$. The longwave radiation flux q_l includes the radiation between
 133 urban surfaces ($q_{l,urban}$) and between urban surfaces and the sky ($q_{l,sky}$), represented as $q_l = q_{l,urban} +$
 134 $q_{l,sky}$.



135

136 **Figure 1: The model design of GUST. In this model, 1D transient conductive heat transfer is considered for**
 137 **urban surfaces the system (e.g., walls, roofs, and ground). They are composed of multiple layers where the**
 138 **thermal properties are uniform and isotropic. All urban surfaces are assumed to be opaque in this study.**

139 In this model, all urban surfaces are represented as triangular facets in STL format, with each triangular
 140 facet treated as a single element. Ray tracing and heat-conduction calculations are performed at the
 141 centroid of each element. The spatial resolution of the simulation can be refined by using smaller
 142 triangular facets, thereby increasing the number of elements. Fig. 6 illustrates the triangulated
 143 representation of the urban surfaces.

144 **2.1. Conduction sub-model**

145 The Monte Carlo random walking method is used to solve the 1D heat conduction ([Talebi et al., 2017](#)).
 146 Compared to finite volume method, this approach is insensitivity to the complexity of urban geometry
 147 and boundary conditions ([Villefranque et al., 2022](#); [Caliot et al., 2024](#)). In the present version, the heat
 148 conduction along the wall span is neglected. The one-dimensional (1D) transient heat conduction
 149 equation is:

$$150 \quad \frac{\partial}{\partial t} T = \alpha \frac{\partial^2 T}{\partial x^2} \quad (2)$$

151 where $\alpha = \frac{k}{\rho c_p}$ is the solid thermal diffusivity and k the thermal conductivity, ρ the density, c_p the
 152 specific heat capacity. The ground, walls and roofs are composed of multiple layers. In the Monte Carlo
 153 random walking method, the heat conduction equation is replaced by finite difference approximation as:

$$154 \quad T(x, t + \Delta t) = P_t T(x, t) + P_{x-} T(x - \Delta x, t + \Delta t) + P_{x+} T(x + \Delta x, t + \Delta t) \quad (3)$$

155 where $P_t = \frac{1}{1+2Fo}$ is defined as probability of time step; $P_{x-} = P_{x+} = \frac{Fo}{1+2Fo}$, where P_{x-} and P_{x+}
 156 respectively represent the probabilities of stepping to the points $(x - \Delta x, t)$ and $(x + \Delta x, t)$. Here,
 157 $Fo = \frac{k\Delta t}{\rho c_p (\Delta x)^2}$ These coefficients are nonnegative probabilistic values and

$$158 \quad P_t + P_{x-} + P_{x+} = 0 \quad (4)$$

159 The Monte Carlo random walking algorithm is schematically illustrated in Fig. 2. The core idea is that
 160 particles walk by following rules:

161 1) Start a random walk at point x .
 162 2) Generating a random number (R) between 0 and 1.

163 3) Determine walking direction by conditions

$$164 \quad \begin{cases} 0 < R < P_{x-}: & x \rightarrow (x - \Delta x) \\ P_{x-} < R < (P_{x-} + P_{x+}): & x \rightarrow (x - \Delta x) \\ (P_{x-} + P_{x+}) < R: & x \rightarrow (x), T(i) = T(i) + T(x, t - \Delta t) \end{cases} \quad (5)$$

165 4) If the next point is not on the boundary repeat step 2 and 3 and if it is on the boundary, record $T(i) =$

166 $T(i) + T$ at the boundary and go to step 1.

167 5) After N random walking, temperature at point x is calculated by

$$168 \quad T(x) = \frac{T(i)}{N} \quad (6)$$

169 When a particle reaches a heat flux, convective or interface boundary, its movement follows the following

170 rules.

171 1) Heat flux boundary

172 When the particle walks to the boundary of heat flux (q), it is bounced back and record the temperature

173 T_{hf} , which is calculate by $T_{hf} = \frac{q\Delta x}{k} + \frac{q}{2k}(\Delta x)^2$.

174 2) Convective boundary

175 The heat flux of a convective boundary is calculated by $q = h(T_w - T_a)$, where h is the heat transfer

176 coefficient and T_w the wall temperature and T_a the air temperature. The wall temperature is calculated

177 by

$$178 \quad T_w = \frac{1}{1 + Bi} T(x - \Delta x) + \frac{Bi}{1 + Bi} T_a \quad (7)$$

179 Where $P_x = \frac{1}{1 + Bi}$, $P_a = \frac{Bi}{1 + Bi}$, $Bi = \frac{h\Delta x}{k}$. When the particle reaches the convective boundary, a new

180 random number R was generated and moves as follows:

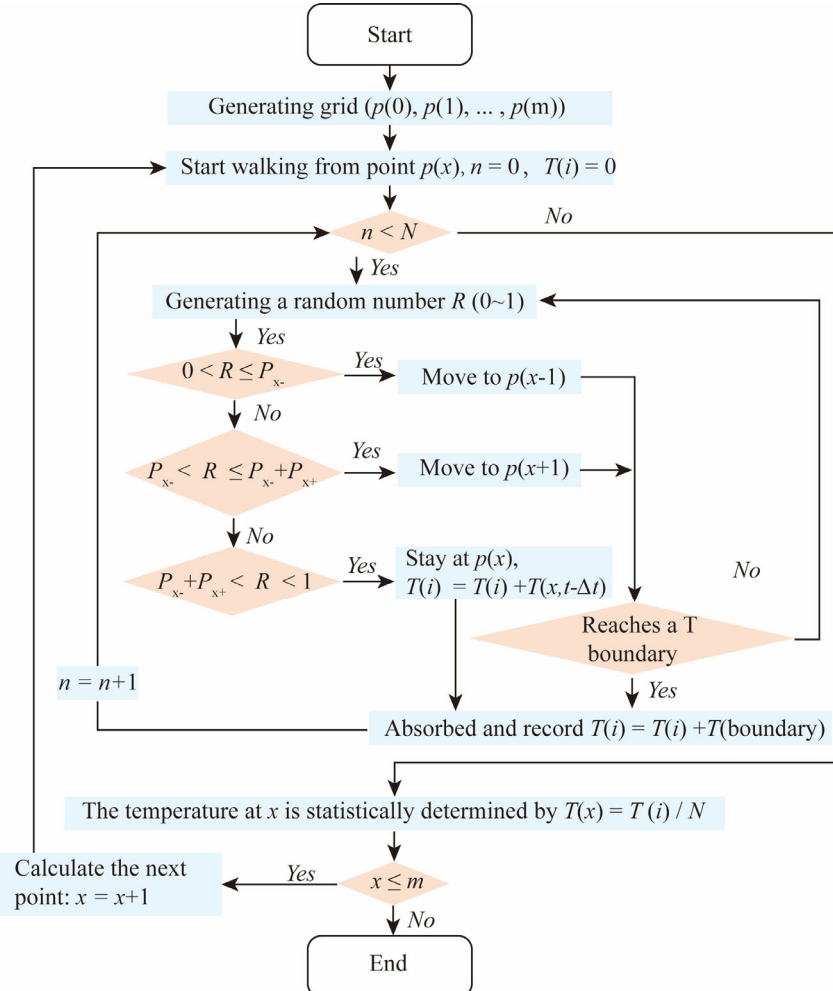
$$181 \quad \begin{cases} 0 < R < P_x: & \rightarrow \text{bounced back} \\ P_x < R < 1: & \rightarrow \text{absorbed by air with } T(i) = T(i) + T_a \end{cases} \quad (8)$$

182 3) Interface between two layers

183 The interface between layers is flux continuity, i.e. the conductive fluxes are equal on both sides of the

184 interface. The heat conductivities on left and right sides of the interface are k_A and k_B . The conductive
 185 heat fluxes on both sides are equal, i.e., $-k_A \frac{dT}{dx} = -k_B \frac{dT}{dx}$. When a particle reaches the interface, it may
 186 be reflected or move to the next layer. A new random number R is generated. The particle moves by
 187 following

188
$$\begin{cases} 0 < R < P_{x-} : & \rightarrow \text{bounced back to layer A} \\ P_{x-} < R < 1 : & \rightarrow \text{move to layer B} \end{cases} \quad (9)$$

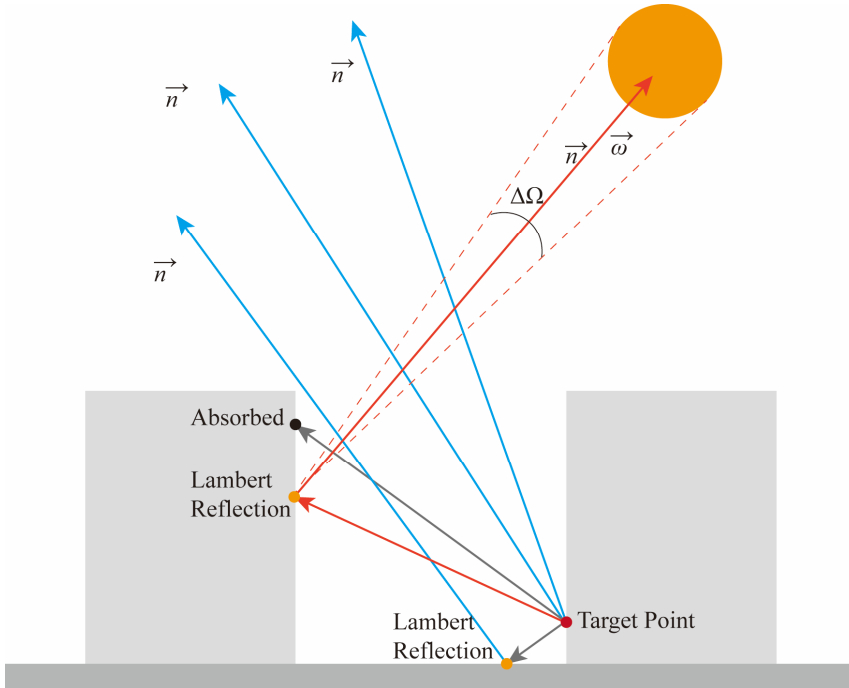


189

190 **Figure 2: Flowchart of the Monte Carlo random walking algorithm for 1D heat conduction. At each point,**
 191 **the particle movement stops after N random walks. Each walk stops when particle either reaches a fixed**
 192 **temperature boundary or remains stationary. Orange diamonds indicate decision points with two possible**
 193 **outcomes (Yes/No).**

194 2.2. Solar radiation sub-model

195 The solar radiation q_s is calculated on each triangular facet using the reverse Monte Carlo Ray Tracing
196 (rMCRT) method, which inherently accounts for both shaded and sunlit areas. In the rMCRT, the ray
197 starts from the target points, instead of starting from the sky or sun in the ray tracing method ([Caliot et](#)
198 [al., 2024](#)). This method ensures that enough photons reach the target point to obtain a statistical result.



200 **Figure 3: Schematic illustration of the reverse MCM ray tracing method for calculating the direct and diffuse**
201 **solar radiation.**

202 The procedure of reverse MCRT is schematically explained in Fig. 3. In total, N photons leave the target
 203 point in random directions (\vec{r}), which is determined by the azimuth θ_a and incidence angle η_a . These
 204 angles are calculated by $\theta_a = 2\pi R_1$ and $\eta_a = \arccos(1 - 2R_2)$, where R_1 and R_2 are random
 205 numbers between 0 and 1.

When a photon reaches the surface, it can be absorbed or reflected via Lambert's law. To determine whether this photon is absorbed, a random number R_{ab} (ranging from 0 ~ 1) is generated. When $R_{ab} > \alpha_s$ (surface albedo), the photon is absorbed by the surface. When $R_{ab} < \alpha_s$, the photon is reflected. All surfaces are considered Lambertian and the direction of reflect solar beam is determined by the azimuth

210 θ_a and incidence angle η_a of that surface. At each reflection, θ_a and η_a are recalculated by
211 regenerating new random numbers.

212 When the photon reaches the “sky” in the direction of \vec{r} , its angle (θ_{ns}) with the reverse solar direction
213 $\vec{\omega_{sun}}$ is calculated. When $\theta_{ns} < \Delta\Omega_d$, that photon is marked as reaching the “Sun”, otherwise, that
214 photon is marked as reaching the “Sky”. The direct ($q_{s,o}$) and diffuse ($q_{s,r}$) solar radiation reaching the
215 target point can then be statistically determined by:

$$216 \quad q_{s,o} = \frac{\pi I_{s,o}}{\Delta\Omega_d N} \sum_{\theta_{ns} < \Delta\Omega_d} |\vec{\omega_{sun}} \cdot \vec{n}| \quad (10)$$

$$217 \quad q_{s,r} = \sum_{\theta_{ns} > \Delta\Omega_d} \frac{I_{s,r}}{N} \quad (11)$$

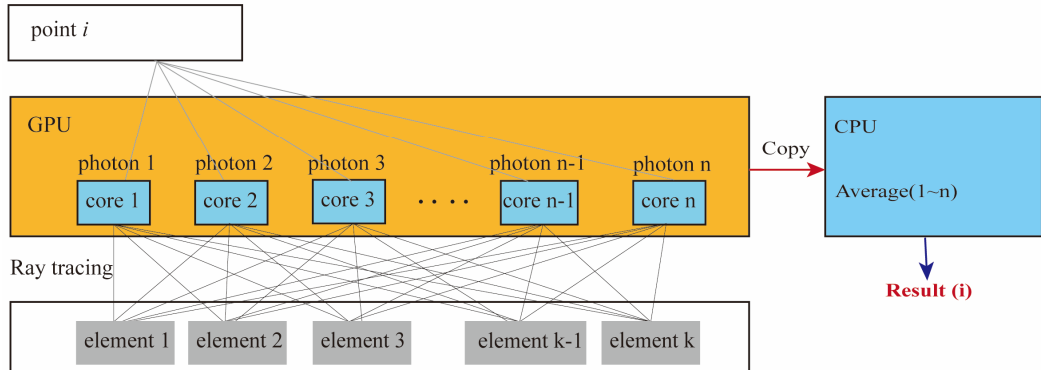
218 where $I_{s,o}$ and $I_{s,r}$ is the direct normal irradiance and diffuse solar radiation. The ratio between the
219 direct and diffuse solar radiation is calculated by the model proposed by ([Reindl et al., 1990](#)).

220 The rMCRT requires a large number of rays to achieve statistically reliable results. To accelerate the
221 simulation, the model is run in parallel on GPUs (Graphics Processing Units) using the CUDA® platform
222 ([Yoshida et al., 2024](#)). The advantage of GPUs is that they have a large number of cores, which enables
223 them to handle many parallel tasks simultaneously. GPUs are particularly well-suited for accelerating
224 MCRT, since each ray tracing operation is independent.

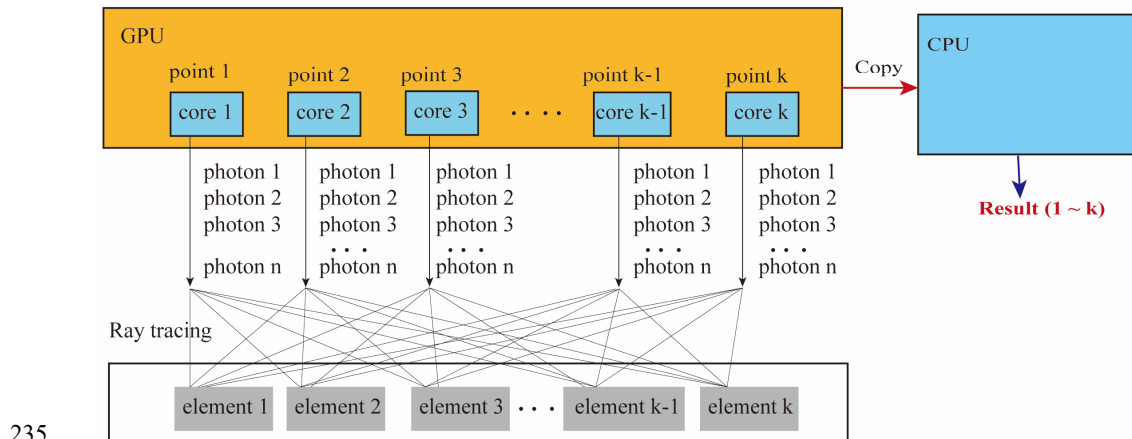
225 The GPU parallel computing is executed using two strategies, depending on the total number of elements.
226 As illustrated in Fig. 4, Strategy 1 calculates the radiative flux point by point, emitting n photons for
227 ray tracing simulation. Each photon is processed in a separate GPU core. Once the ray tracing process is
228 complete, the results from the GPU cores are copied to the CPU, where radiative flux at each point is
229 calculated. Strategy 2 calculates the radiative flux for all points simultaneously, with each GPU core
230 computing the flux for a single point. The ray tracing of n photons is performed iteratively on the GPU.

231 The advantage of Strategy 1 is the efficient utilization of GPU cores when the number of points and
232 elements is small. However, its disadvantage is that it requires a large amount of memory when the
233 number of points is large. In contrast, Strategy 2 requires significantly less memory and only transfers
234 data to the CPU once, making it highly efficient when the number of points and elements is large.

(a) Strategy 1



(b) Strategy 2



235

236 **Figure 4: Two strategies for GPU parallel computing. (a) The ray tracing is conducted point by point. For**
 237 **each point, n photons are emitted. Each GPU core calculates one photon. (b) The ray tracing is conducted**
 238 **for all points at one time. Each GPU core calculates one point. The ray tracing of n photons is performed**
 239 **iteratively within the GPU core.**

240 The space angle of the Sun ($\Delta\Omega_d$) and the number of photons (N) can significantly affect the accuracy of
 241 reverse MCM. To evaluate this influence, a series of test cases are conducted, in which the direct solar
 242 radiation at a ground point is calculated. The solar radiation on the open ground can be calculated
 243 theoretically, as there is no shading from buildings.

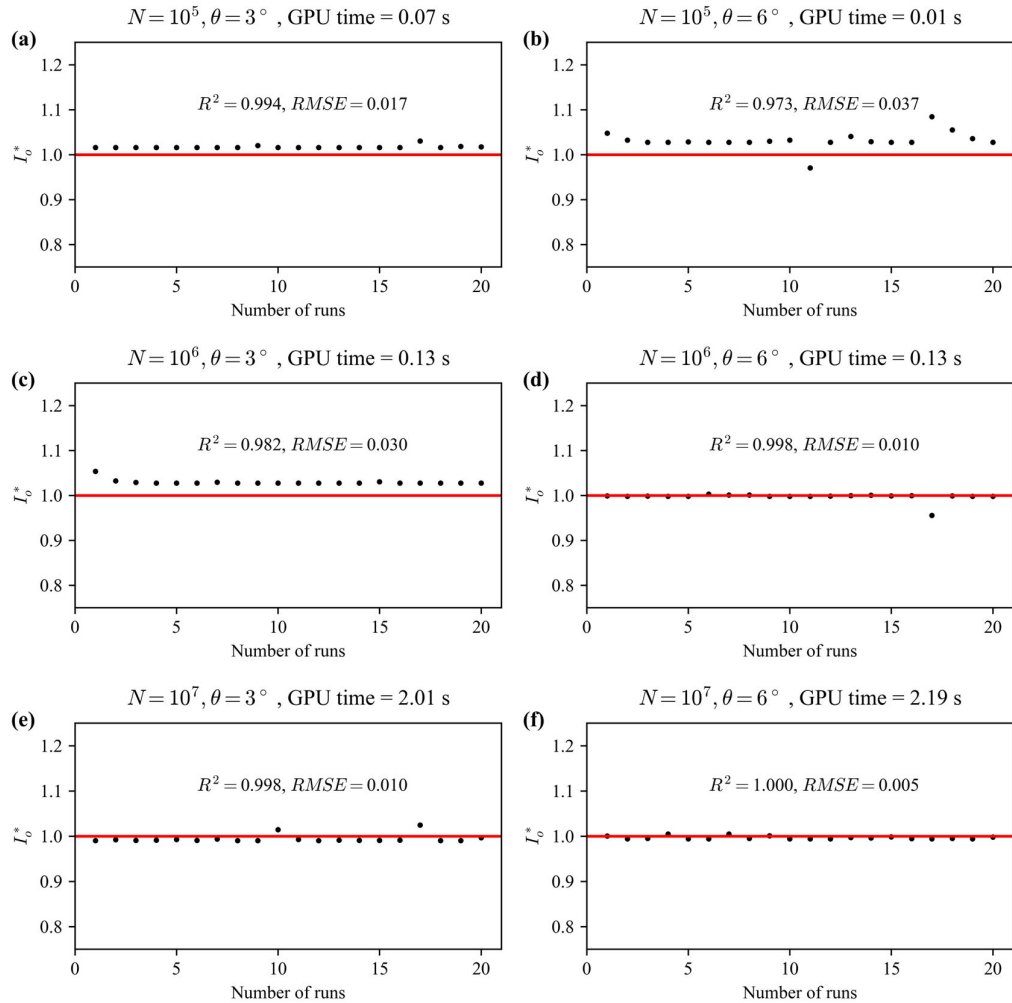
244 Figure 5 shows the errors of simulations using different values of N and $\Delta\Omega_d$. The simulation time of
 245 each case is also indicated in that figure. When the number of photons is increased from $N = 10^5$ to
 246 $N = 10^7$, the simulation time increases from 0.05s to 1.15s, which is an increase of 23 times. The

247 relatively slow increase in simulation time is a result of the parallel computing capabilities of the GPU.

248 In each scenario, the model was run 20 times to observe the difference between each run.

249 A small $\Delta\Omega_d$ reduce the photon number reaching the Sun, thus increasing the error, where the $\Delta\Omega_d$ is
250 calculated from a 2D angle θ as $\Delta\Omega_d = 2\pi(1 - \cos(\theta))$. For example, the error in cases with $\theta = 3^\circ$
251 greater than that in cases with $\theta = 6^\circ$. A larger number of photons is needed to compensate for this error.
252 For example, the case with $\theta = 3^\circ$ and $N = 10^7$ shows acceptable accuracy. However, the case with
253 $\theta = 6^\circ$ shows a comparable accuracy when $N = 10^6$ and takes less simulation time.

254 In the subsequent simulations, $\theta = 6^\circ$ and $N = 10^6$ are applied to balance accuracy and simulation
255 time.



256

257 **Figure 5: Numerical errors of direct solar radiation estimation using Monte Carlo method. The simulated**
 258 **solar radiation ($I_{o,sim}$) is normalized by the true value ($I_{o,true}$) and is expressed by ($I_o^* = \frac{I_{o,sim}}{I_{o,true}}$), where $I_o^* =$**
 259 **1.0 represents an exact reproduction of the solar radiation. The test cases use different space angles of sun**
 260 **$\Delta\Omega_d = 2\pi(1 - \cos(\theta))$ and photon numbers (N). The red lines represent the true value, and dots represent**
 261 **the simulated data.**

262 **2.3. Longwave radiation sub-model**

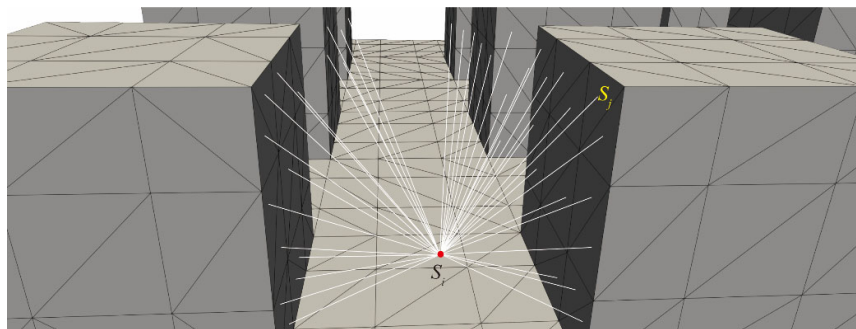
263 The view factors between the surfaces, as well as from the surfaces to the sky, are also calculated using
 264 the Monte Carlo ray tracing model, as illustrated in Fig. 6. The urban surfaces are divided into multiple
 265 triangular elements N_{ur} . The view factor from element S_i to element S_j , denoted as $F_{i,j}$, is calculated
 266 by emitting N photons from the centroid of element S_i . The algorithm then counts the number of
 267 photons $n_{i,j}$ that reach element S_j . Finally, the view factor $F_{i,j}$ is calculated by $F_{i,j} = n_{i,j}/N$. The sky
 268 view factor is also determined in this approach by treating the sky as an urban surface.

269 The longwave radiative heat exchange between the surfaces, as well as from the surfaces to the sky, is
 270 calculated by:

271

$$q_l = F_{i,sky} \varepsilon (R_{l,in} - \sigma T_i^4) + \varepsilon \sigma \sum_{j=1}^{j=N_{ur}} F_{i,j} (T_j^4 - T_i^4) \quad (12)$$

272 where ε is the material emissivity, σ is Stefan–Boltzmann constant ($= 5.67 \times 10^{-8}$) (W m⁻² K⁻⁴), $R_{l,in}$ is
 273 the downward longwave radiation from the sky, $F_{i,sky}$ is the sky view factor of element S_i . The surface
 274 temperature from the previous step (T_i and T_j) is used to calculate the longwave radiative heat exchange.



276 **Figure 6: Schematic illustration of how view factors are calculated between urban surface elements.**

277 **2.4. Outdoor convective sub-model**

278 GUST does not calculate urban airflow; instead, it uses empirical formulas to calculate the outdoor
279 convective heat flux as follows:

280
$$q_{c,out} = U_f h_{out} (T_{w,out} - T_{a,out}) \quad (13)$$

281 where $T_{a,out}$ is the outdoor air temperature in the canopy layer, U_f is the wind speed, and convective
282 heat transfer coefficient $h_{out} = 4.5 \left(\frac{ws}{m^3 K} \right)$ is adopted.

283 The wind speed above the urban canopy layer (UCL) is calculated by a logarithm wind profile:

284
$$U(z) = \frac{u_*}{\kappa} \ln \left(\frac{z + z_0}{z_0} \right) \quad (14)$$

285 where $z_0 = 0.1H$ based on the estimation of ([Grimmond and Oke, 1999](#)).

286 The wind speed within the UCL is assumed to be uniform and is calculated by the model by Bentham
287 and Britter ([Bentham and Britter, 2003](#)). This model estimates the in-canopy velocity (U_c) based on the
288 frontal area density (λ_f) as follows:

289
$$\frac{U_c}{u_*} = \left(\frac{2}{\lambda_f} \right)^{0.5} \quad (16)$$

290 Here, the friction velocity (u_*) depends on the urban morphology and is estimated using the following
291 functions ([Yuan et al., 2019](#)):

292
$$\begin{cases} u_* = 0.12U_{2H}, & \text{for } (\lambda_f > 0.4) \\ u_* = 6.7U_{2H}^3 - 6.4U_{2H}^2 + 1.7U_{2H} + 0.03, & \text{for } (\lambda_f < 0.4) \end{cases} \quad (17)$$

293 where U_{2H} is the wind speed at a height of $2H$ above the ground, and H is the building height.

294 The air temperature in UCL is assumed to be uniform and calculated by the urban canopy model ([Yuan
295 et al., 2020](#)). This model estimates the in-canopy temperature based on the exchange velocity U_E and
296 sensible heat flux $q_{c,out}$.

297
$$T_c = \frac{1}{D_c} \frac{q_{c,out}}{U_{2H}(1 - \lambda_p)} \left(1 - 0.12 \left(\frac{2}{\lambda_f} \right)^{0.5} \right) + T_{a,2H} \quad (18)$$

298 where $D_c = 17.183$, is a heat capacity constant of the air, $T_{a,2H}$ is the air temperature above the roof
299 level, λ_p is the plan area density. Bentham and Britter ([Bentham and Britter, 2003](#)) suggested that the
300 U_E can be calculated by:

301

$$\frac{U_E}{u_*} = \left(\frac{U_{2H} - U_c}{u_*} \right)^{-1} \quad (19)$$

302 The $q_{c,out}$ is calculated by the temperature from previous time step.

303 **2.5. Indoor sub-model**

304 The indoor side uses a convective boundary condition given by $q_{in} = h_{in}(T_{w,in} - T_{a,in})$, where $T_{a,in}$ is
305 the indoor air temperature, $T_{w,in}$ is the wall temperature on indoor side. The indoor heat transfer
306 coefficient $h_{in} = 13.5 \frac{W}{m^2 K}$ accounts for both natural convection and longwave radiative heat flux.

307 For air-conditioned rooms, the indoor air temperature is assumed to be constant at $T_{a,in} = 26$ °C. In
308 contrast, for naturally ventilated rooms, the indoor air temperature is assumed to be equal to the in-canopy
309 air temperature, represented as $T_{a,in} = T_c$.

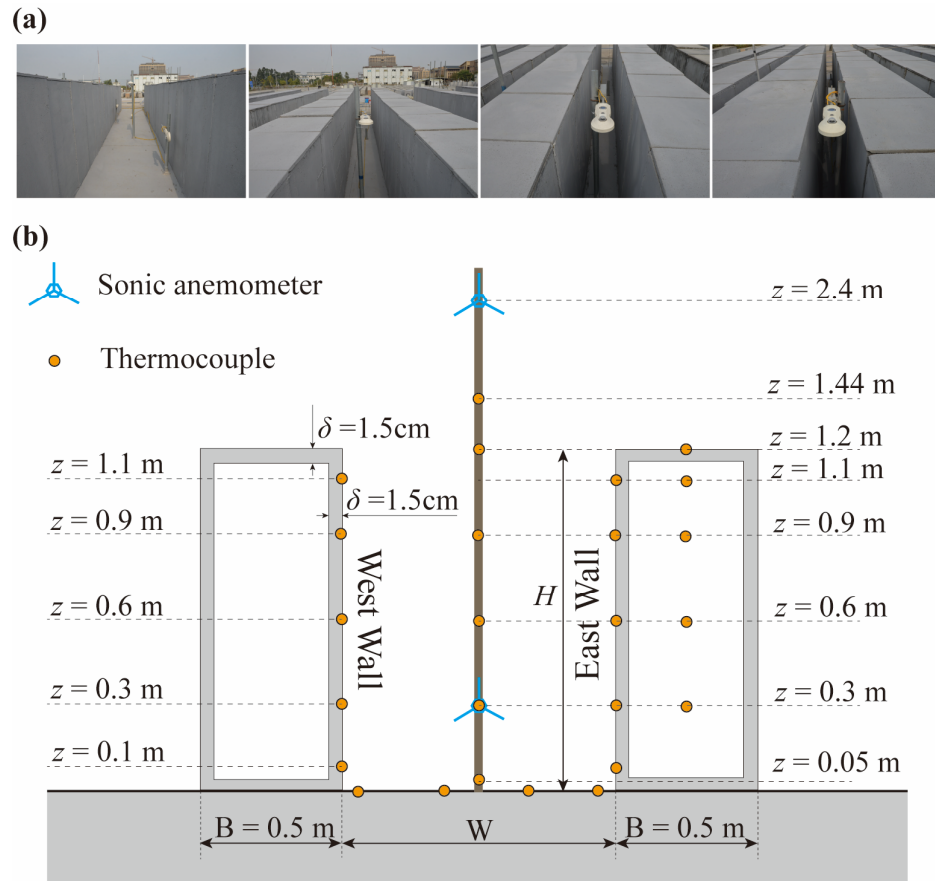
310 **3. Model validation and assessment**

311 **3.1. SOMUCH measurement**

312 The model is validated by cross-compare with the SOMUCH measurement, which is a scale outdoor
313 field measurement conducted in Guangzhou, P.R. China (23°1' N, 113°25' E) ([Hang and Chen, 2022](#);
314 [Hang et al., 2025](#); [Wu et al., 2024](#)). This measurement provides a quality database for evaluating urban
315 climate models ([Hang et al., 2024](#); [Chen et al., 2025](#)). The campaign conducted from 29th Jan to 1st
316 Feb 2021 is used. In that campaign, both surface and air temperatures were measured at high resolution,
317 making it an ideal database for validating current models.

318 The geometry of the building blocks and measurement points are plotted in Fig. 7. In that measurement,
319 the urban buildings are modeled by hollow concrete blocks with a size of 0.5 m × 0.5 m × 1.2 m and a
320 thick of 0.015 m. The blocks are arranged to form street canyons with four different aspect ratios, i.e.,
321 H/W = 1, 2, 3, 6. Each row consists of 24 blocks and has a length of L = 12 m. In the experiment, the
322 surface and air temperatures are measured using thermocouples (Omega, TT-K-36-SLE, Φ0.127 mm and

323 TT-K- 30-SLE, $\Phi 0.255$ mm). The wind speeds inside and above the street canyon are measured using
 324 sonic anemometers (Gill WindMaster). The incoming longwave and solar radiation are measured using
 325 weather stations (RainWise PortLog). The thermal characteristics of the concrete and ground are listed
 326 in Table 1.



327

328 **Figure 7: Photograph of the SOMUCH experiment (a). The geometry of concrete blocks and measurement**
 329 **points in SOMUCH (b). The thermocouples are used to measure the surface temperature and air temperature.**
 330 **The sonic anemometers are used to measure wind speed.**

331

332 **Table 2. Thermal properties of the building material. The emissivity is for the longwave radiation and albedo**
 333 **is for the solar radiation.**

| Material | Density ρ (kg m ⁻³) | Conductivity k (W m ⁻¹ K ⁻¹) | Specific Heat Capacity c_p (J kg ⁻¹ K ⁻¹) | Emissivity ϵ | Albedo α |
|----------|---|--|---|--------------------------|--------------------|
| Concrete | 2420 | 2.073 | 618 | 0.87 | 0.24 |

334

335 **3.2. Cross comparison of the roof temperature**

336 The surface temperature model is validated by cross-comparing with SOMUCH measurement. Many
 337 factors affect the accuracy of the model, including the radiation, convective and conduction. To
 338 separately investigate these factors, the temperatures at roofs are first validated because the total radiative
 339 flux of roof is only influenced by the incoming longwave and solar radiation. The shading effect of other
 340 blocks can be ignored as the block heights are uniform. Therefore, the accuracy of conductive and
 341 convective sub-models can be separately evaluated.

342 The accuracy of this model is quantitatively evaluated by two statistical parameters, the root mean square
 343 error (RMSE), and coefficient of determination (R^2). The RMSE and R^2 of u_x^* are calculated by:

$$344 \quad \text{RMSE} = \sqrt{\frac{1}{n} \sum_{i=1}^n (O_i - P_i)^2} \quad (21)$$

$$345 \quad R^2 = 1 - \frac{\sum_{i=1}^n (O_i - P_i)^2}{\sum_{i=1}^n (O_i - \bar{O}_i)^2} \quad (22)$$

346 where O_i represents the measured values, P_i is the simulated values, \bar{O}_i is the mean of the measured
 347 values, and n is the number of data points.

348 The wind speed at roof level is needed to calculate the outdoor convective flux of roofs. In SOMUCH
 349 measurement, the wind speed was measured above the roof and at a height of $2H$. The wind speed at
 350 roof level is estimated by a logarithm wind profile as:

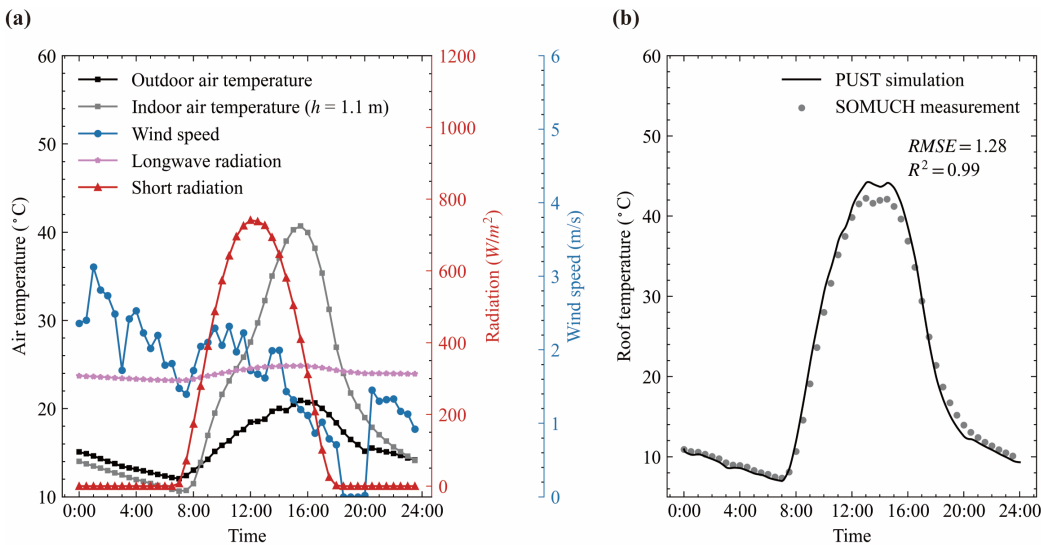
351

$$U(z) = \frac{u_*}{\kappa} \ln \left(\frac{z + z_0}{z_0} \right) \quad (23)$$

352 where $z_0 = 0.1H$ based on the estimation of (Grimmond and Oke, 1999). The wind velocity at roof
 353 level ($z = H$) can be calculated by $\frac{U_H}{U_{2H}} = 0.787$. The outdoor air temperature, incoming solar and
 354 longwave radiation, are from the weather station ($z = 2H$).

355 For the indoor side, the radiative flux between indoor surfaces is ignored in this model. Only the
 356 convective flux is modeled. The convective velocity is assumed to be 3 m/s and CHTC is assumed to be
 357 4.5 for indoor side. Data from the indoor measurement point at $H = 1.1$ m is used. That point is the
 358 nearest measurement point to the roof.

359 Figure 8(a) plotted the measurement data that was used to drive the model. During the measurements,
 360 the building model was enclosed, leading to the development of very high indoor temperatures. Therefore,
 361 the measured indoor air temperature was used as an input for the validation simulation. Fig. 8(b) shows
 362 the roof surface temperatures from measurement and simulation. Generally, the roof surface temperatures
 363 are well reproduced by the model, because the R^2 is 0.99 and RMSE is 1.28. The large discrepancy is
 364 found around noon. The model slightly overestimates the roof temperature. The comparison of roof
 365 temperatures shows that the conductive and convective sub-models are reliable.



366

367 **Figure 8: Weather data on the measurement date (29 January 2021) is shown in (a). Panel (b) compares roof**
 368 **surface temperatures from simulation and measurement, where points denote measured data and lines denote**

369 simulated data.

370 **3.3. Cross comparison of the wall temperature**

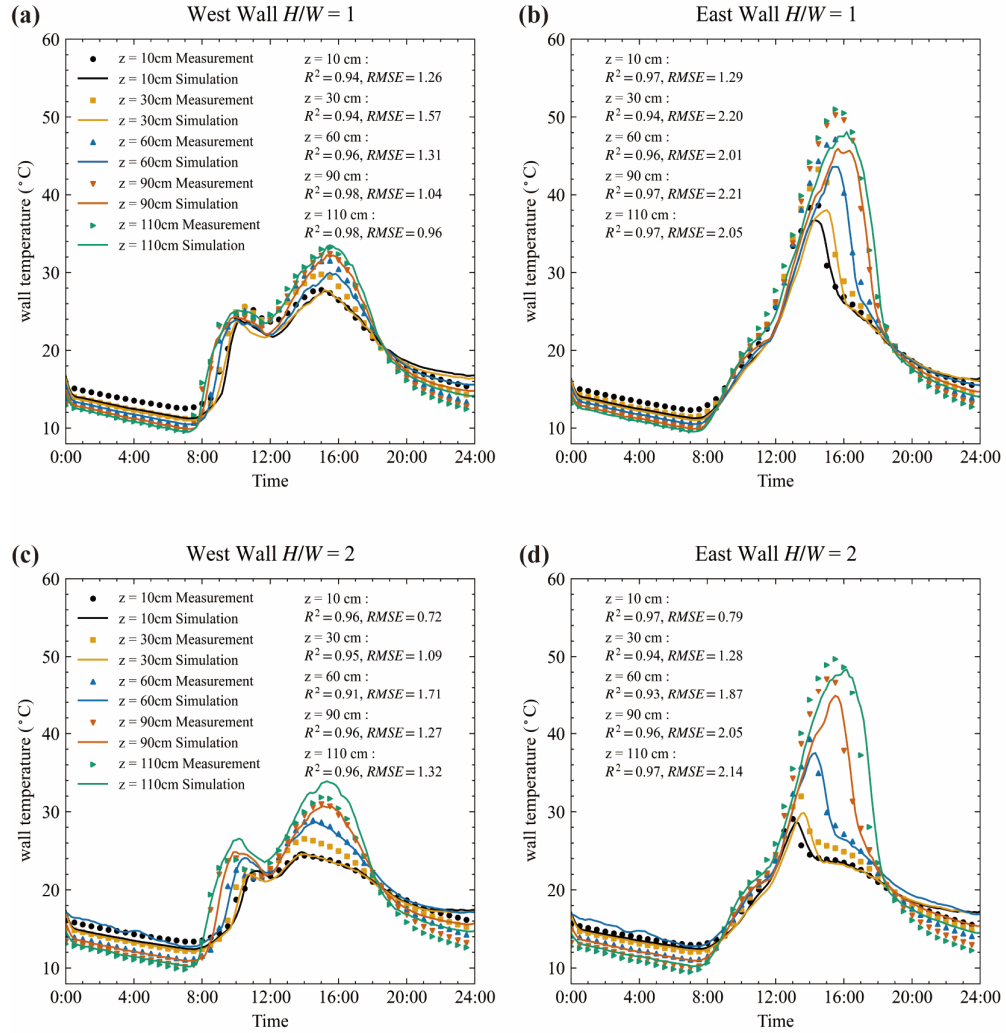
371 The temperatures at walls are more complicated than those at the roof because the buildings change the
372 radiative fluxes and wind speeds in street canyons. The radiative fluxes need to be accurately modelled
373 as they are the main energy input and have a large impact on the surface temperature. To avoid the
374 influence of air temperature and wind speed modeling, the canyon air temperature, wind speed, and
375 indoor temperature are from the measurement. The air temperatures are measured from multiple heights.
376 For the convective flux modelling, the nearest measured air temperatures are used. The wind speeds from
377 the sonic anemometer in the street canyon ($z = 0.3$ m) are used to calculate the convective flux at outdoor
378 side. The driving data are plotted in Appendix A.

379 The east and west walls are defined by taking street canyon center as the origin point. The street direction
380 is tilted from north toward east by 25° . Therefore, the west and east walls are roughly defined to
381 distinguish them. The street orientation has been modeled in our model and will not cause additional
382 discrepancy.

383 Figures 9 and 10 show the comparison of wall temperatures from simulation and measurement. For each
384 surface, multiple points are compared to avoid the influence of localized anomalies and to ensure that
385 the evaluation reflects the overall wall-temperature behavior. Generally, the wall temperatures are well
386 reproduced, particularly their variation trend. The peak hours are well reproduced. For example, there
387 are two temperature peaks for the west wall. The first one is around 10:00 and the second is around 16:00.
388 Both simulation and measurement show the same occurring time.

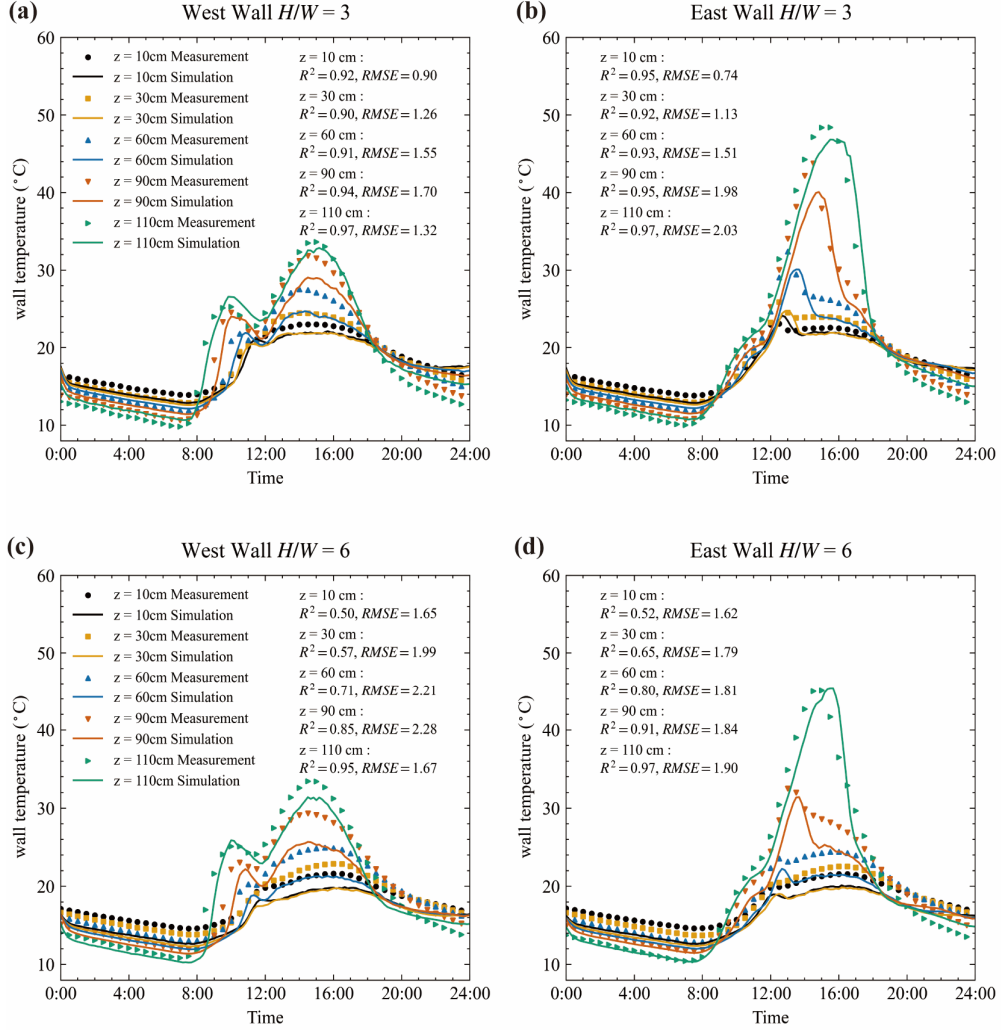
389 To quantify model performance, the coefficient of determination (R^2) and root-mean-square error
390 (RMSE) were calculated and marked in each sub-figure. Except for the $H/W = 6$ case, the R^2 values
391 exceeded 0.9 for all walls, confirming a strong correlation between simulation and measurement. For
392 $H/W = 6$, R^2 is lower because of nighttime underestimation, although the RMSE remains within the
393 same range as the other cases (1.6 $^\circ\text{C}$ to 2.2 $^\circ\text{C}$). The main reason for this discrepancy is that wall
394 temperatures in deep street canyons ($H/W = 6$) show only a slight increase compared to the air
395 temperature, due to minimal sunlight penetration into the canyon. Under these conditions, wall

396 temperatures become particularly sensitive to convective and longwave radiative fluxes, which amplifies
 397 the impact of small modeling uncertainties.



398

399 **Figure 9: Wall temperature comparison between simulation and measurements for street canyons with aspect**
 400 **ratios of $H/W = 1.0$ and 2.0 . Surface temperatures were measured on 29 January 2021. The root mean square**
 401 **error (RMSE) and coefficient of determination (R^2) are calculated and shown. Symbols denote measurements,**
 402 **while lines indicate simulations. The left panel corresponds to west side walls and the right panel to east side**
 403 **walls.**



404

405 **Figure 10: Wall temperature comparison between simulations and measurements, as in Figure 9, but for street**
 406 **canyons with aspect ratios of $H/W = 3$ and 6.**

407 **3.4. Cross comparison of the ground temperature**

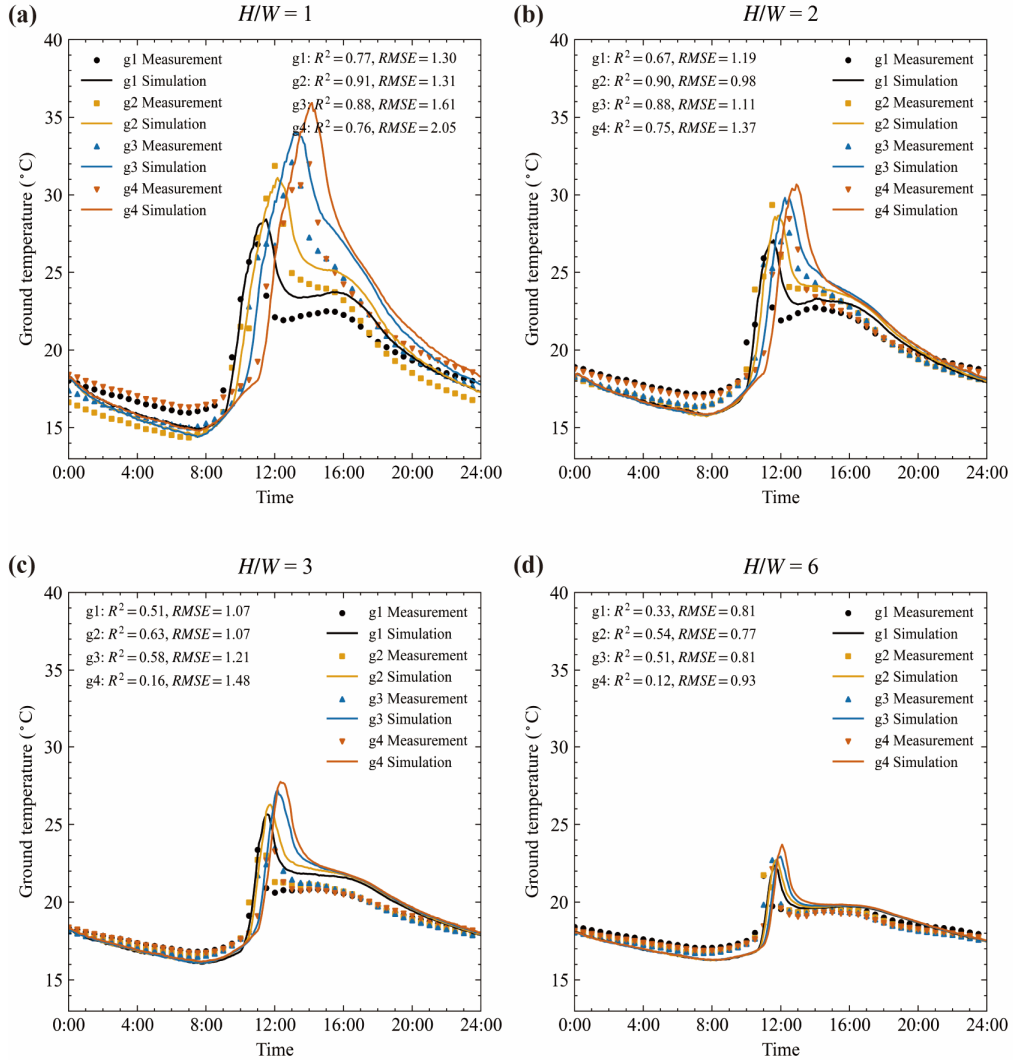
408 The surface temperatures of the ground are heavily influenced by heat storage. During the day, heat is
 409 conducted to deeper layers and stored there. At night, this stored heat is released. Therefore, the initial
 410 temperature field and boundary conditions are critical for accurately modeling surface temperatures. In
 411 this study, an adiabatic boundary condition is applied at a depth of 0.5 m below the ground surface. The
 412 soil material is divided into three layers with thicknesses of 0.2 m, 0.15 m, and 0.15 m. All three layers
 413 are assumed to be made of concrete. The thermal properties in Table 1 are used. The underground

414 temperatures are measured by thermocouples with three depths of 5 cm, 10 cm, and 20 cm, as plotted in
415 Appendix A. In this study, we used only the measured underground temperatures at 0:00 to initialize the
416 underground temperature field. It is important to note that the available soil temperatures were measured
417 in open ground rather than under street canyons. This difference may lead to discrepancies in modeling
418 ground surface temperatures.

419 Figure 11 shows the ground surface temperatures from measurement and simulation. The ground surface
420 temperatures are measured at four locations: g1, which is close to west wall; g4, which is close to east
421 wall; and g2 and g3, which are situated in the middle of the streets. Generally, the temperature variations
422 are well reproduced by the model. For example, peak temperatures occur sequentially from g1 to g4 due
423 to the movement of the building's shadow. This phenomenon is observed in both simulations and
424 measurements.

425 The accuracy of ground temperatures is lower than that of the wall temperatures in terms of R^2 . For
426 example, in $H/W = 2$, the R^2 values for temperatures at the west wall range from 0.91 to 0.97, while
427 those at the ground range from 0.67 to 0.90. However, the ground temperatures can be considered well
428 modeled because the RMSE for ground temperatures is smaller than that for wall temperatures. Using
429 $H/W = 2$ as an example, the RMSE values for the west wall range from 0.69 to 1.71 °C, while those for
430 the ground range from 0.98 to 1.37 °C. This difference between the R^2 and RMSE values is due to the
431 ground temperature increase being much lower than that of the walls because of shading, particularly in
432 deep street canyons.

433 Uncertainties in the input data may also contribute to the discrepancies between simulation and
434 measurement. First, the thermal properties of soil can differ significantly from those of concrete blocks.
435 Secondly, the initial temperature is measured in surrounding area, rather than in street canyons. Thirdly,
436 since the same initial temperature field is used for all four points, the model is unable to reproduce the
437 differences between points at night.



439 **Figure 11: Ground temperature comparison between the simulation and measurement results at street canyon**
 440 **aspect ratio of $H/W = 1.0, 2.0, 3.0$, and 6.0 . Surface temperatures are measured on 29th Jan 2021. The root**
 441 **mean square error (RMSE), and coefficient of determination (R^2) are calculated and plotted. The points**
 442 **represent measured data and lines represent the simulated data.**

443

444 **3.5. Surface energy balance analysis**

445 The surface temperature comparison indicates that model uncertainties arise from various factors. To
 446 identify the main factors impacting the model accuracy, the energy balance of wall surface is analyzed.

447 The heat fluxes of solar (Q_K), longwave radiation (Q_L), convection (Q_H), and conduction (Q_G) of outer
448 surface of walls satisfy the following equation:

449
$$Q_K + Q_L + Q_G + Q_H = 0 \quad (24)$$

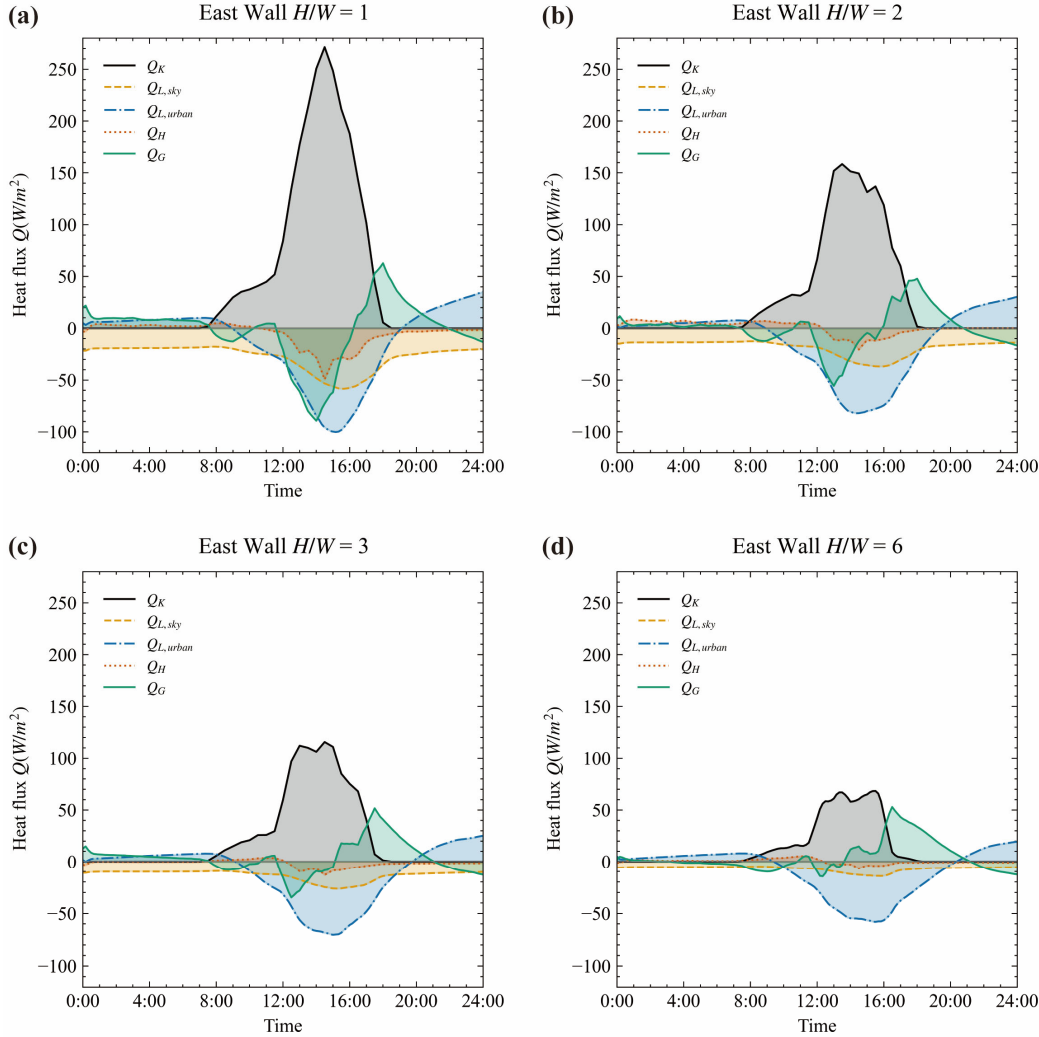
450 Here, the longwave heat flux Q_L is divided into two parts as the heat exchange between wall to sky
451 ($Q_{L,sky}$) and to other urban surfaces ($Q_{L,urban}$), expressed as $Q_L = Q_{L,sky} + Q_{L,urban}$. This analysis aims
452 to determine whether it is necessary to model the longwave heat exchange between urban surfaces, which
453 requires substantial computational resources.

454 Figures 12 and 13 show the heat fluxes of walls in the simulation. The heat fluxes of east and west walls
455 are averaged from five measurement points on each. Our previous work ([Mei et al., 2025](#)) demonstrated
456 that a Monte Carlo ray-tracing approach accurately predicts incident solar radiation. In that study, we
457 compared the albedo of the urban canopy layer and of street canyons across a range of urban layouts with
458 in-situ measurements, achieving excellent agreement.

459 In all cases, longwave radiative heat exchange between urban surfaces plays an important role in the
460 energy balance, particularly at high aspect ratios. The longwave radiative fluxes from sky only contribute
461 a small amount of total longwave radiative flux in $H/W = 6$, as shown in Fig. 12(d) and Fig. 13(d). The
462 shading effect of buildings creates heterogeneous surface temperatures within the urban canopy layer.
463 The large temperature differences between surface elements contribute a large portion of the total heat
464 flux. This highlights the necessity for accurate modeling of longwave heat exchange between urban
465 surfaces, even though it demands significant computational resources.

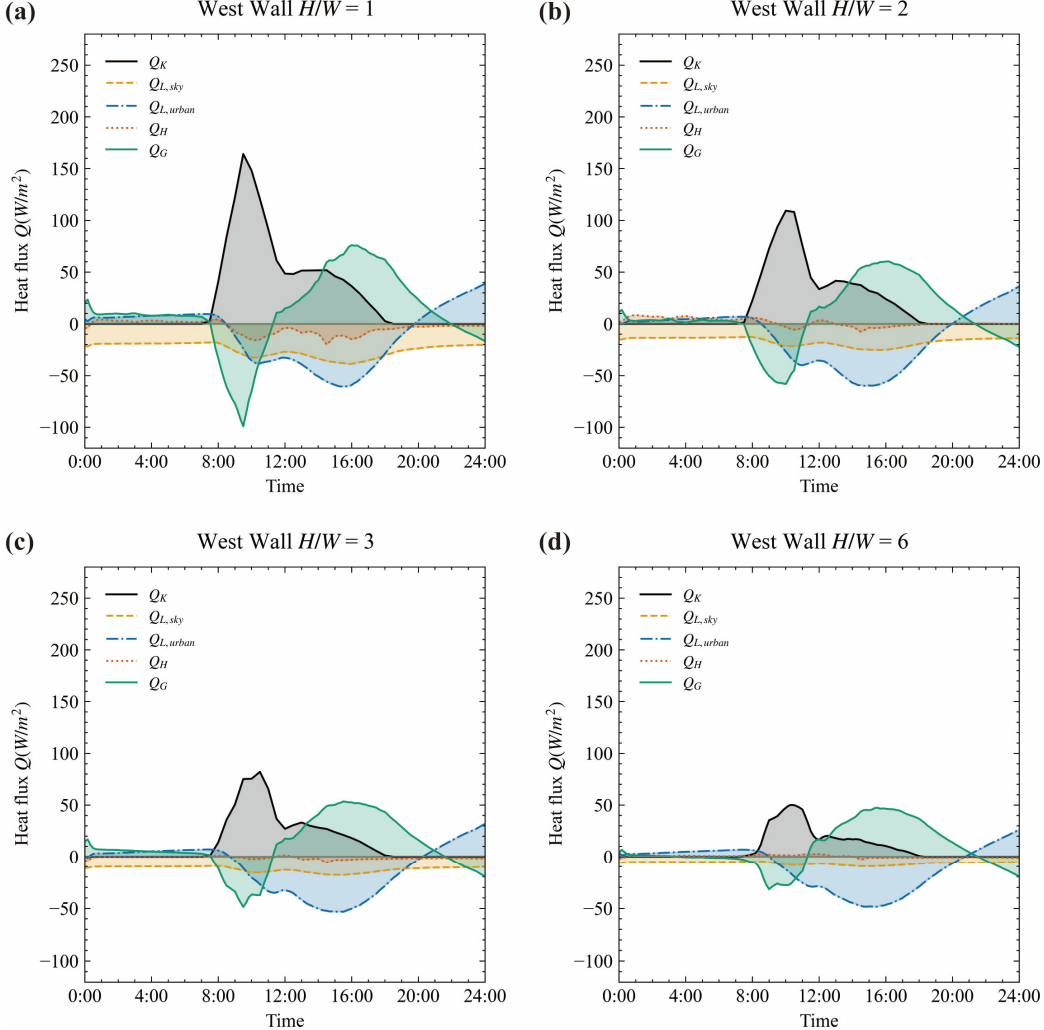
466 The conductive heat flux also contributes a large portion of the total heat flux. It is negative in the
467 morning and positive in the afternoon, meaning that heat is stored in the building block during the
468 morning and released in the afternoon. In the reduced scale experiment, buildings were represented by
469 airtight hollow concrete blocks. Due to the lack of ventilation, the indoor air temperature can rise to 40°
470 C under an outdoor air temperature of 20°C, as shown in Appendix A. This indicates that the indoor air
471 can also absorb, store, and release a considerable amount of heat. Therefore, accurately modeling indoor
472 air temperature is essential for effective surface temperature modeling.

473 The convective contributes a smaller amount of the total heat flux. In high aspect ratio cases ($H/W = 3$
 474 and 6), the convective heat fluxes are almost negligible. This is due to the weak wind in the deep street
 475 canyons. In this model, the surface convective heat flux is directly calculated from the wind speeds in
 476 street canyons. This assumption may underestimate the convective flux, especially since natural
 477 convection occurs under weak wind conditions (Fan et al., 2021).



478

479 **Figure 12: Diurnal heat fluxes at the east side walls from the simulation. The heat fluxes of solar (Q_K),**
 480 **longwave radiation (Q_L), convection (Q_H), and conduction (Q_G) are at the outer surface of walls.**



481

482 **Figure 13: Diurnal heat fluxes at the west side walls from the simulation. The heat fluxes of solar (Q_K),**
 483 **longwave radiation (Q_L), convection (Q_H), and conduction (Q_G) are at the outer surface of walls.**

484 **4. Application to real urban configuration**

485 To demonstrate the model's applicability to complex geometries, we simulated a neighborhood
 486 containing 40 buildings within an area of $350\text{ m} \times 200\text{ m}$. Building geometries were imported as STL
 487 files comprising approximately 2.3×10^4 triangular surface meshes. Surface temperatures were calculated
 488 on the triangular surface elements, as shown in Fig. 6, with shortwave fluxes resolved by a Monte Carlo
 489 ray-tracing scheme using 1×10^5 photons. The solar position is updated at 30-min intervals to capture both
 490 diurnal and shading variations. Transient heat conduction simulations were performed for 24 h with a

491 10-min time step (600 s) on 29 January 2021, consistent with the validation case. Downward solar
492 radiation, longwave radiation, wind speed, and air temperature were prescribed from the SOMUCH
493 measurements.

494 The simulation ran on a local workstation with an NVIDIA RTX 5090D GPU and completed in 26.6 h,
495 comprising a view-factor calculation (4.2 h), solar-radiation computation (22.2 h), and coupled heat-
496 transfer analysis (0.2 h).

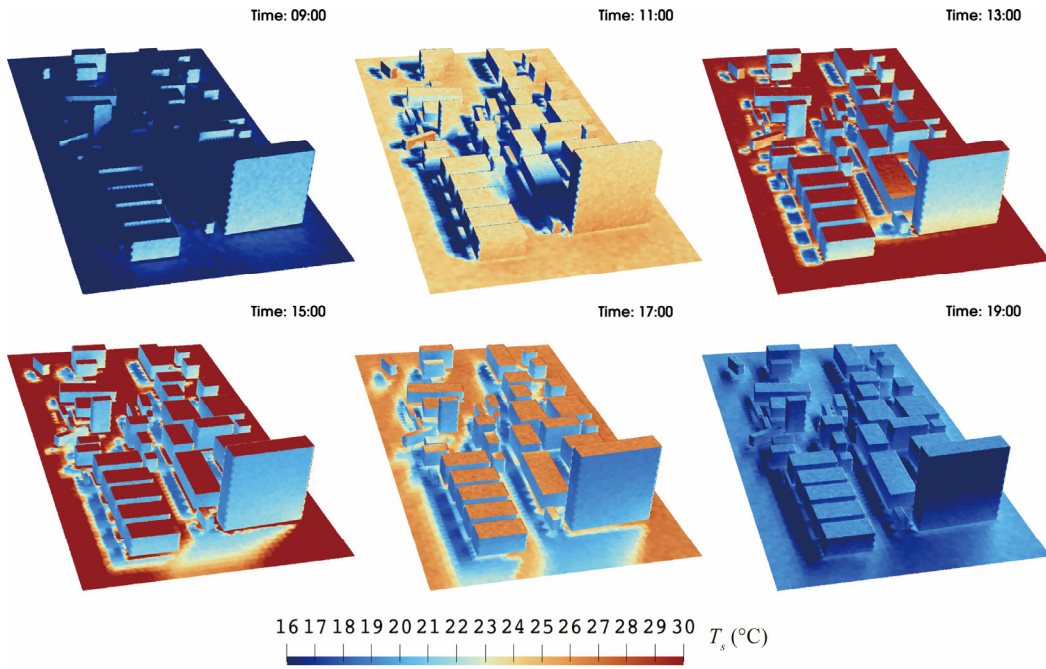
497 For this demonstration, material-specific reflectance was neglected and a uniform albedo of 0.24 was
498 applied to all urban surfaces. Walls and roofs were modeled as three concrete layers of 0.10 m each (total
499 thickness = 0.30 m), while the ground comprised 0.35 m (0.15 m + 0.15 m + 0.05 m) with an adiabatic
500 bottom boundary. For all layers, thermal properties were fixed to concrete values of thermal conductivity
501 $k = 2.0 \text{ W m}^{-1}\text{K}^{-1}$, density $\rho = 2420 \text{ kg m}^{-3}$, and specific heat capacity $c_p = 618 \text{ J kg}^{-1}\text{K}^{-1}$. All
502 model inputs are consolidated into a single YAML configuration file, which specifies the simulation
503 parameters, weather forcing, geometry paths, surface albedo, and material thermal properties for easy
504 reproducibility. The buildings are assumed to be naturally ventilated, with the indoor and outdoor air
505 temperatures being the same. The thermal characteristics of concrete are assumed to be the same as in
506 the SOMUCH experiment.

507 The surface temperatures are calculated in three steps: 1) calculate the solar radiative flux of each point
508 by rMCRT; 2) calculate the view factors between the elements using rMCRT; 3) calculate the surface
509 temperatures using Monte Carlo random walking. All three steps are processed in parallel on GPU. The
510 weather data measured on 29th Jan 2021 during the SOMUCH experiment is used as the driving input.
511 The surface temperatures are calculated from 0:00 to 24:00, with a time step of 30 minutes.

512 The simulation results were exported in vtk format and visualized using ParaView. Fig. 14 presents the
513 surface temperature distributions at 09:00, 11:00, 13:00, 15:00, 17:00, and 19:00. The movement of
514 building shadows and their influence on surface temperatures are clearly visible in these contours,
515 illustrating the diurnal heating and cooling cycle. These visualizations demonstrate that the model can
516 represent complex building geometries and can be applied to real urban environments.

517 The energy balance analysis of the SOMUCH experiment indicates that convective heat transfer plays

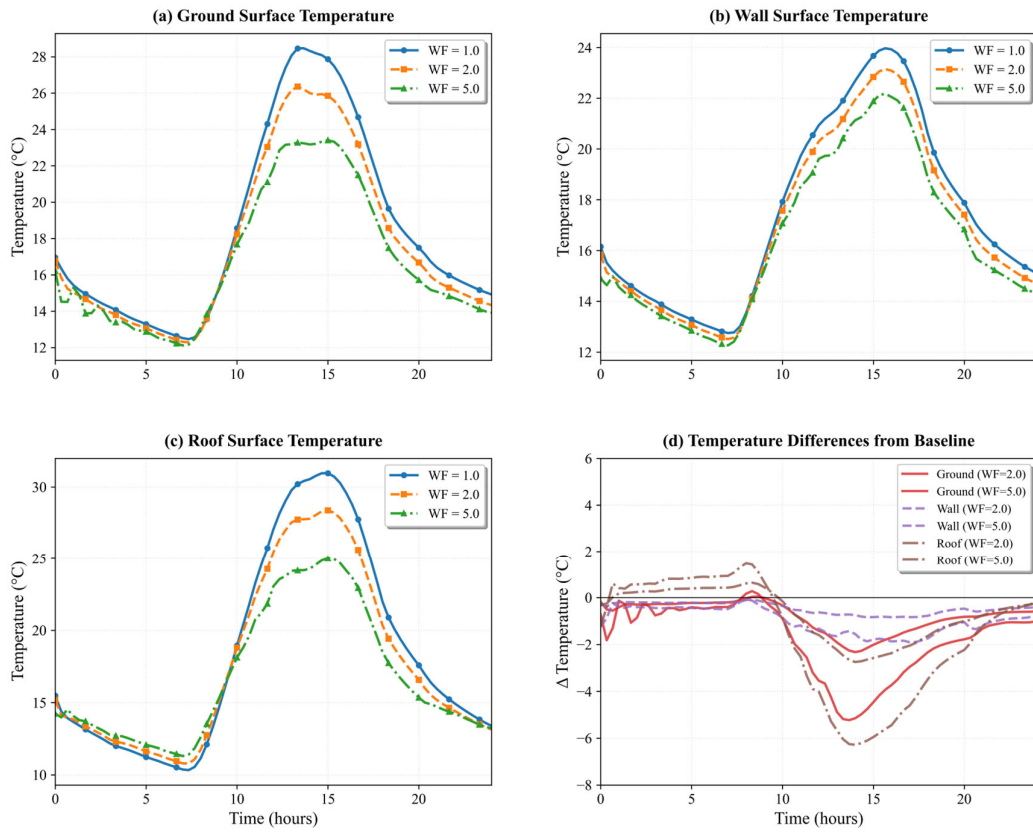
518 only a minor role. However, due to the experiment's reduced scale and limited local wind speeds, it
519 remains uncertain whether this conclusion holds at full scale or under higher wind speed conditions.



521 **Figure 14: Simulation results show the evolution of surface temperature for the complex building geometries**
522 **at 09:00, 11:00, 13:00, 15:00, 17:00, and 19:00. These snapshots capture the diurnal heating and cooling cycle,**
523 **highlighting morning warming, peak midday temperatures, and the evening decline.**

524 To further assess the role of the convective model, a wind sensitivity analysis was performed for the real
525 urban configuration. The baseline wind speed ($WF = 1.0$) was measured on 29 January 2021, the same
526 day used for the validation cases. Wind speeds were then systematically increased by factors of 2.0 and
527 5.0 relative to the baseline to evaluate their influence on urban surface temperatures. The resulting
528 average surface temperatures of the ground, walls, and roof are shown on Fig. 15. The temperature
529 evolution in Fig. 15 (a)–(c) demonstrates that increasing the wind factor from $WF = 1.0$ to 5.0
530 progressively lowers surface temperatures across all urban elements. Fig. 15 (d) quantifies the
531 temperature differences relative to the baseline scenario ($WF = 1.0$), revealing cooling effects of up to
532 6 °C, with the most pronounced reductions occurring during peak heating hours. Among the three
533 surfaces, the roof exhibits the greatest sensitivity to wind variations, followed by the ground and then the
534 walls.

535 These results highlight that, at full scale and under high-wind conditions, convective processes can exert
 536 a much stronger influence on urban surface temperatures than indicated by the scaled SOMUCH
 537 experiment. Therefore, future studies are needed to better quantify and model convective effects across
 538 a broader range of wind speeds and length scales. Moreover, under weak-wind conditions, natural
 539 convection becomes especially important, particularly when the temperature difference between the wall
 540 and the atmosphere grows large ([Fan et al., 2021](#); [Mei and Yuan, 2021](#)). However, this natural-convective
 541 effect may not be significant in the scaled SOMUCH experiment.



542
 543 **Figure 15. Wind-sensitivity analysis of urban surface temperatures showing (a) ground, (b) wall, and (c) roof**
 544 **temperature evolution under different wind factors (WF = 1.0, 2.0, 5.0), and (d) temperature differences**
 545 **relative to the baseline (WF = 1.0). The baseline wind speed was measured on 29 January 2021, the same day**
 546 **used for the model-validation cases.**

547 **5. Limitations and future work**

548 This model is a building-resolved urban surface temperature model, focusing on detailed neighborhood-
549 scale processes. Therefore, its application to full city-scale simulations remains limited by computational
550 cost and is currently best suited for neighborhood-scale. The first version focuses on the complex
551 radiative exchange in densely built urban areas. The parameters and assumptions are validated against
552 the idealized scaled outdoor experiment, which uses homogeneous building materials with consistent
553 albedo and thermal characteristics. Glazing and green infrastructure are not included in this experiment.
554 The SOMUCH project is currently measuring the impact of glass and green infrastructure. The next
555 version will expand its capabilities to capture complex urban materials, such as urban trees, green walls,
556 and glass curtain walls, to better represent real urban configurations. Other limitations include:

- 557 • All reflections are assumed to be Lambertian. While this assumption works well for the SOMUCH
558 measurements, where concrete is used for all urban surfaces, it may not fully capture the reflective
559 properties of other materials with different surface textures, such as glass or vegetation.
- 560 • The high-resolution wall temperature simulation still requires a significant amount of time to
561 complete, even with parallel computation on GPUs. This is due to the large number of rays ($N =$
562 10^6) required for accurate solar radiation modeling. For each point, the simulation takes about 1
563 second to finish. However, as the number of test points increases, the overall computational time
564 grows substantially.
- 565 • The dynamic indoor air temperature is not included in this model. It assumes that the indoor air
566 temperature is equal to the outdoor air temperature for a natural ventilated room. This assumption
567 may lead to discrepancies, particularly in situations where indoor temperatures differ from outdoor
568 conditions due to factors such as heat sources, insulation, or limited ventilation.
- 569 • The participation of the urban atmosphere is ignored in this study. In the scaled measurements,
570 longwave radiation travels much shorter distances to adjacent surfaces, which reduces the influence
571 of atmospheric effects compared to real-world urban environments.

572 **6. Conclusions**

573 This study introduces a GPU-accelerated Urban Surface Temperature model (GUST), which computes

574 radiation using Monte Carlo ray tracing and solves heat conduction with a one-dimensional Monte Carlo
575 random-walk approach. To meet the substantial computational demands of these Monte Carlo
576 simulations, the model employs GPU-based parallel computing for efficient processing. GUST is
577 validated against the high-resolution, scaled outdoor experiment SOMUCH, which provides detailed
578 spatial and temporal measurements.

579 The radiative heat flux is simulated using a reverse Monte Carlo Ray Tracing method, which allows for
580 the accurate reproduction of multiple reflections in high-density urban areas. The sensitivity test shows
581 that $10^5 \sim 10^6$ rays are required for each point to accurately model the solar radiation. This large amount
582 of ray tracing can only be achieved using GPU parallel computing. The Monte Carlo method is also used
583 to solve the couple heat transfer using random walking algorithms, which is suitable for GPU-based
584 coding.

585 The comparison with the SOMUCH experiment shows that the transient surface temperatures on roofs,
586 walls and the ground are well reproduced. A relatively large discrepancy is observed in cases with high
587 building density, where the wall temperatures are highly sensitive to convective and longwave radiative
588 fluxes. The surface energy balance analysis shows that longwave radiation exchange between urban
589 surfaces plays a critical role across all building densities. In contrast, convective heat flux only plays a
590 significant role in high-density cases. In future versions, the simulation of convective heat flux could be
591 improved by simulating urban airflow.

592 Lastly, this model is implemented to solve the surface temperatures on complex urban buildings, which
593 are composed of a total of 2.3×10^4 surface elements. The GPU allows simultaneous simulation of
594 heat transfer and view factors across all elements, enabling high-fidelity simulations in real urban
595 configurations with complex geometries. The current version focuses on the radiation-conduction-
596 convection coupled heat transfer coupled in complex geometries. Future developments will prioritize the
597 integration of complex glazing systems and green infrastructure in urban environments.

598

599 **Code availability**

600 The SOMUCH measurement data are available upon request. The development of GUST, model
601 validation, and visualization in this study were conducted using Python 3.8 with CUDA. The source code,
602 supporting data, and simulation results presented in this paper are archived on Zenodo at
603 <https://doi.org/10.5281/zenodo.17138571> and are freely accessible for research purposes under the
604 Creative Commons Attribution 4.0 International (CC BY 4.0) license.

605

606 **Author contributions**

607 SM designed the study, developed the code, conducted the analysis. SM and GC prepared the manuscript
608 draft. GC and JH collected and shared SOMUCH measurements for the purpose of model validation. GC,
609 JH and TS supported the model implementation and data analysis. All have read and accepted the
610 manuscript for submission.

611

612 **Acknowledgement**

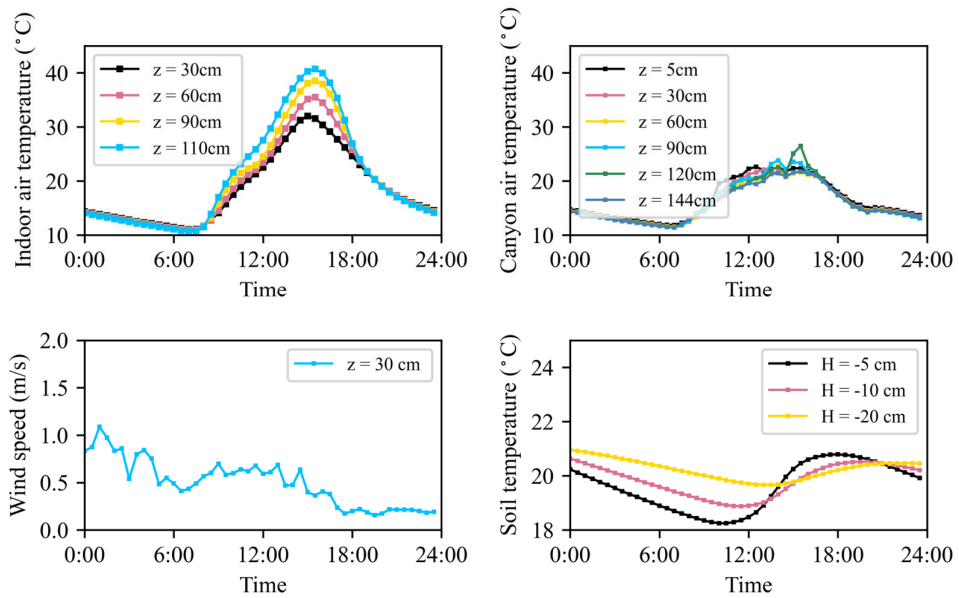
613 This research is supported by National Natural Science Foundation of China (Grant No. 42305076,
614 W2421048, U2442212), Natural Science Foundation of Guangdong Province, China (Grant No.
615 2024A1515010173) and Overseas Postdoctoral Talents 2023 Programme (Grant No. BH2023009). Dr.
616 Shuo-Jun Mei and Dr. Ting Sun are supported by an International Exchanges grant from the Royal
617 Society (Grant No. IEC\NSFC\242040) and National Natural Science Foundation of China (Grant No.
618 W2421048).

619

620 **Appendix A. Indoor and outdoor air temperatures in SOMUCH measurement**

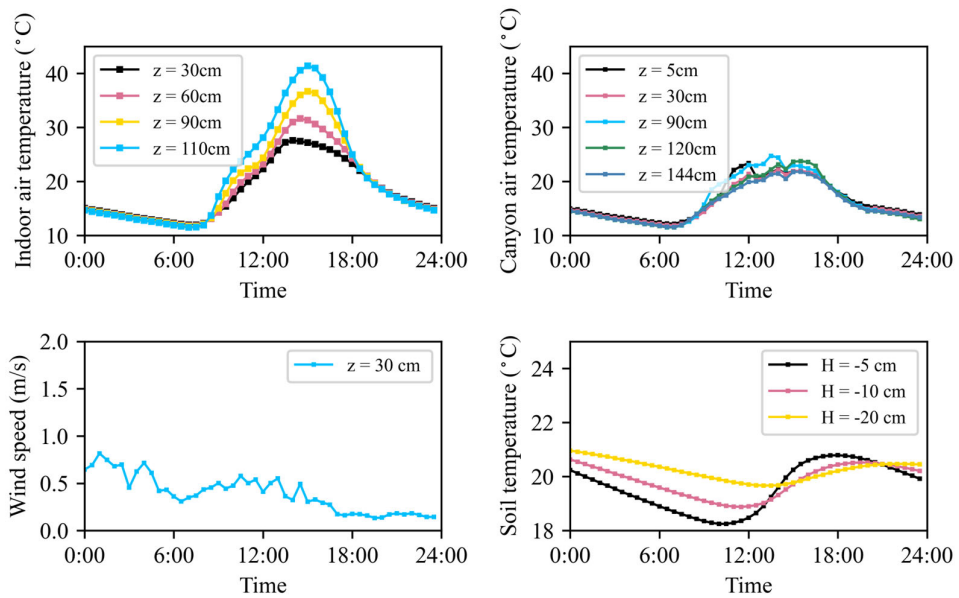
621 The indoor and outdoor air temperatures at different levels in the SOMUCH measurement are plotted in
622 Fig. A1. These air temperatures serve as input data for the validation cases.

(a) $H/W = 1$



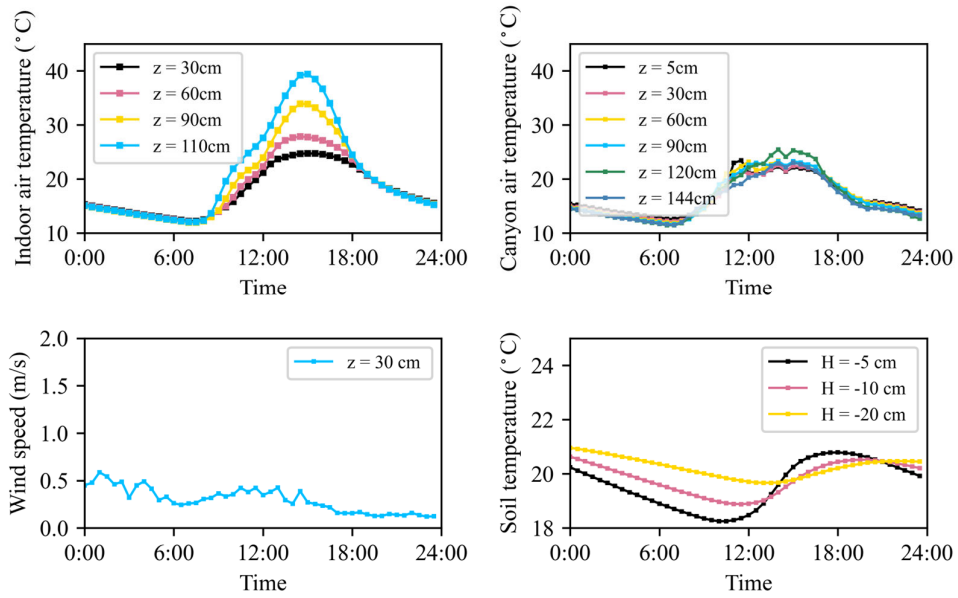
623

(b) $H/W = 2$



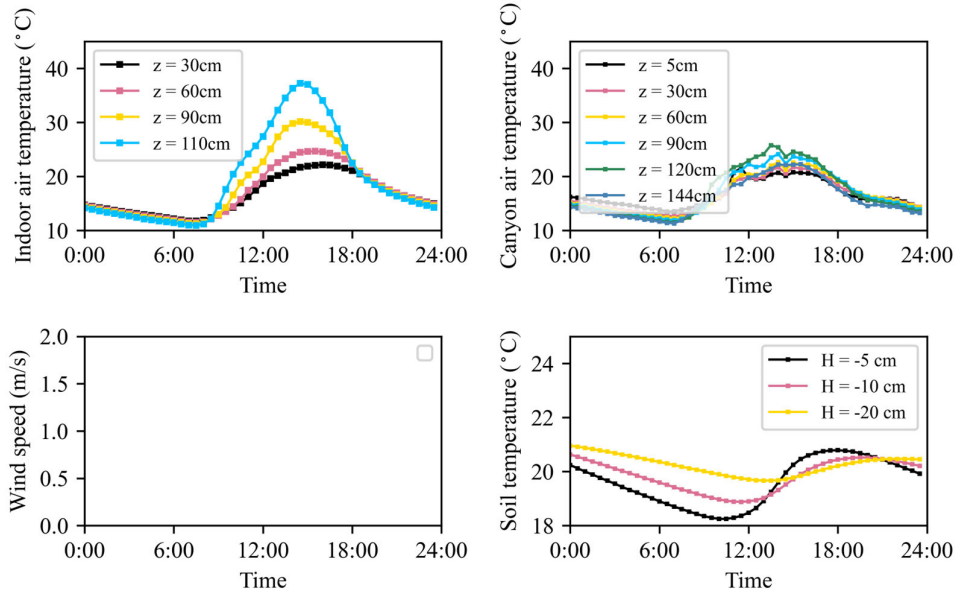
624

(c) $H/W = 3$



625

(d) $H/W = 6$



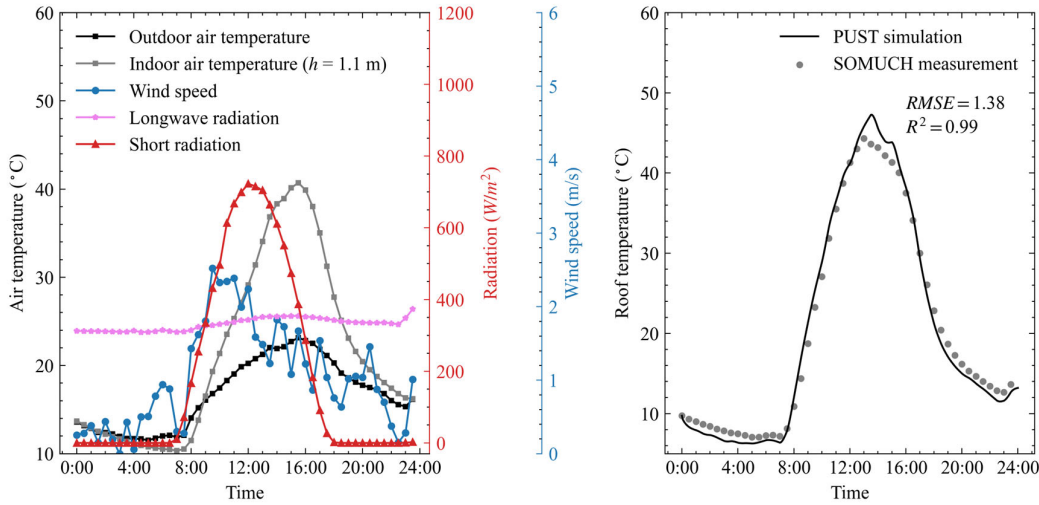
626

627 **Figure A1: Indoor, outdoor air temperatures, and wind speeds in street canyons that are measured on 29th**
 628 **Jan 2021. The wind speeds in the street canyon of $H/W = 6$ were not measured because the sonic anemometer**
 629 **cannot be installed in such a narrow street. The outdoor air temperatures measured at $z = 60$ cm in $H/W = 2$**
 630 **are unusual, due to an instrument failure.**

631 **Appendix B. Sensitivity test for other days**

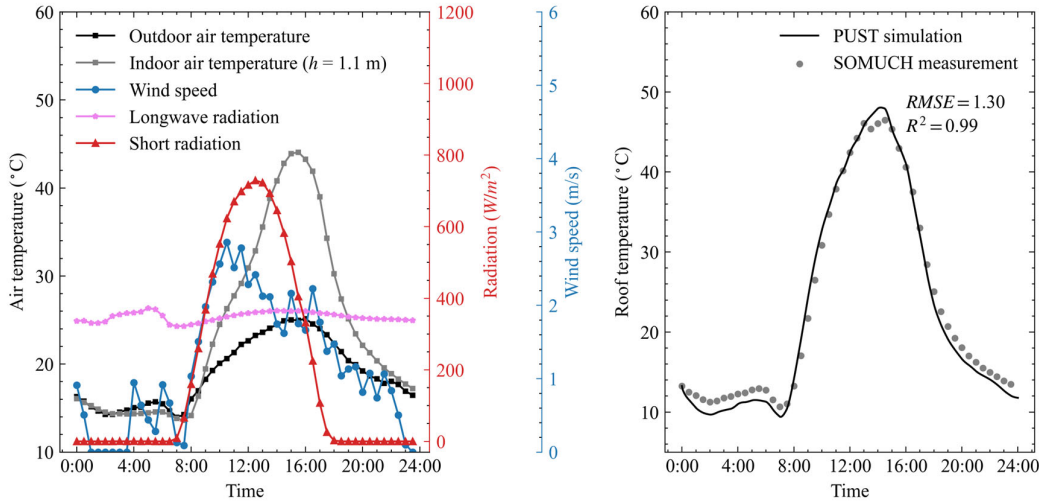
632 To further validate the model, we also compared the simulated roof temperatures with measurements over three
 633 consecutive days, from 30 January to 1 February 2021, similar to the analysis presented in Fig. 8. The results are
 634 shown in Fig. A2, which demonstrates excellent agreement between simulated and observed roof temperatures. By
 635 using multiple consecutive days, this comparison minimizes potential bias arising from the single day's weather
 636 conditions.

637 **(a) 30th Jan 2021**



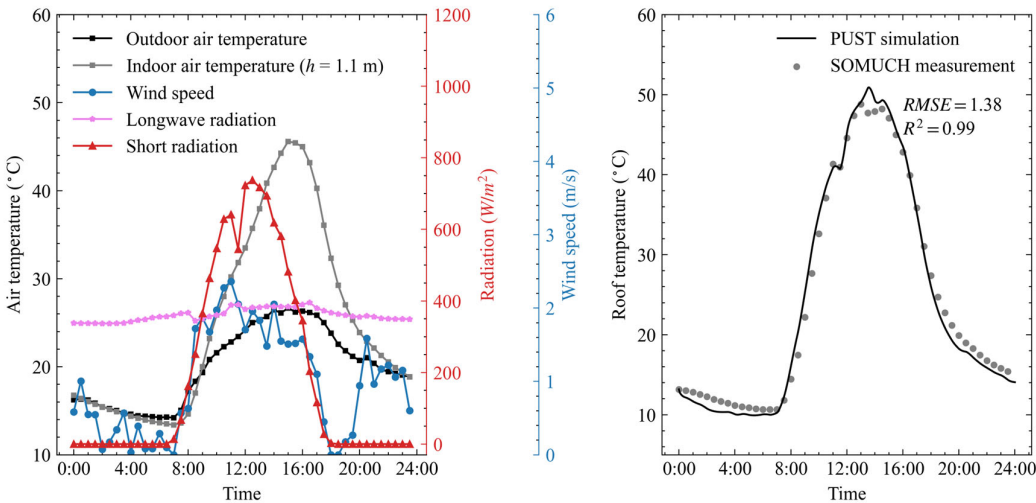
638

639 **(b) 31st Jan 2021**



640

641 **(c) 1st Feb 2021**



642

643 **Figure A2: Weather data from 30 January to 1 February 2021 are shown in the left panels. The right panels**
 644 **compare roof-surface temperatures from simulation and measurement, with points representing observations**
 645 **and lines representing simulated values.**

646 References

647 Bentham, T. and Britter, R.: Spatially averaged flow within obstacle arrays, *Atmospheric Environment*,
 648 37, 2037-2043, [https://doi.org/10.1016/S1352-2310\(03\)00123-7](https://doi.org/10.1016/S1352-2310(03)00123-7), 2003.

649 Caliot, C., d'Alençon, L., Blanco, S., Forest, V., Fournier, R., Hourdin, F., Retailleau, F., Schoetter, R.,
 650 and Villefranque, N.: Coupled heat transfers resolution by Monte Carlo in urban geometry including
 651 direct and diffuse solar irradiations, *International Journal of Heat and Mass Transfer*, 222, 125139,
 652 <https://doi.org/10.1016/j.ijheatmasstransfer.2023.125139>, 2024.

653 Carmeliet, J. and Derome, D.: How to beat the heat in cities through urban climate modelling, *Nature*
 654 *Reviews Physics*, 6, 2-3, 10.1038/s42254-023-00673-1, 2024.

655 Chen, G., Mei, S.-J., Hang, J., Li, Q., and Wang, X.: URANS simulations of urban microclimates:
 656 Validated by scaled outdoor experiments, *Building and Environment*, 272, 112691,
 657 <https://doi.org/10.1016/j.buildenv.2025.112691>, 2025.

658 Ebi, K. L., Capon, A., Berry, P., Broderick, C., de Dear, R., Harenith, G., Honda, Y., Kovats, R. S., Ma,
 659 W., Malik, A., Morris, N. B., Nybo, L., Seneviratne, S. I., Vanos, J., and Jay, O.: Hot weather and
 660 heat extremes: health risks, *The Lancet*, 398, 698-708, [https://doi.org/10.1016/S0140-6736\(21\)01208-3](https://doi.org/10.1016/S0140-6736(21)01208-3), 2021.

662 Eingrüber, N., Domm, A. S., Korres, W., and Schneider, K.: Simulation of the heat mitigation potential
 663 of unsealing measures in cities by parameterizing grass grid pavers for urban microclimate modelling
 664 with ENVI-met (V5), *EGUphere*, 2024, 1-25, 10.5194/egusphere-2024-697, 2024.

665 Fan, Y., Zhao, Y., Torres, J. F., Xu, F., Lei, C., Li, Y., and Carmeliet, J.: Natural convection over vertical

666 and horizontal heated flat surfaces: A review of recent progress focusing on underpinnings and
667 implications for heat transfer and environmental applications, Physics of Fluids, 33, 101301,
668 10.1063/5.0065125, 2021.

669 Feng, J., Gao, K., Khan, H., Ulpiani, G., Vasilakopoulou, K., Young Yun, G., and Santamouris, M.:
670 Overheating of Cities: Magnitude, Characteristics, Impact, Mitigation and Adaptation, and Future
671 Challenges, Annual Review of Environment and Resources, 48, 651-679,
672 <https://doi.org/10.1146/annurev-environ-112321-093021>, 2023.

673 Forouzandeh, A.: Prediction of surface temperature of building surrounding envelopes using holistic
674 microclimate ENVI-met model, Sustainable Cities and Society, 70, 102878,
675 <https://doi.org/10.1016/j.scs.2021.102878>, 2021.

676 Grimmond, C. S. B. and Oke, T. R.: Aerodynamic properties of urban areas derived from analysis of
677 surface form, Journal of Applied Meteorology, 38, 1262, 10.1175/1520-
678 0450(1999)038<1262:APOUAD>2.0.CO;2, 1999.

679 Grimmond, C. S. B., Blackett, M., Best, M. J., Barlow, J., Baik, J.-J., Belcher, S. E., Bohnenstengel, S.
680 I., Calmet, I., Chen, F., Dandou, A., Fortuniak, K., Gouvea, M. L., Hamdi, R., Hendry, M., Kawai,
681 T., Kawamoto, Y., Kondo, H., Krayenhoff, E. S., Lee, S.-H., Lorian, T., Martilli, A., Masson, V.,
682 Miao, S., Oleson, K., Pigeon, G., Porson, A., Ryu, Y.-H., Salamanca, F., Shashua-Bar, L., Steeneveld,
683 G.-J., Tombrou, M., Voogt, J., Young, D., and Zhang, N.: The International Urban Energy Balance
684 Models Comparison Project: First Results from Phase 1, Journal of Applied Meteorology and
685 Climatology, 49, 1268-1292, <https://doi.org/10.1175/2010JAMC2354.1>, 2010.

686 Grimmond, C. S. B., Blackett, M., Best, M. J., Baik, J.-J., Belcher, S. E., Beringer, J., Bohnenstengel, S.
687 I., Calmet, I., Chen, F., Coutts, A., Dandou, A., Fortuniak, K., Gouvea, M. L., Hamdi, R., Hendry,
688 M., Kanda, M., Kawai, T., Kawamoto, Y., Kondo, H., Krayenhoff, E. S., Lee, S.-H., Lorian, T.,
689 Martilli, A., Masson, V., Miao, S., Oleson, K., Ooka, R., Pigeon, G., Porson, A., Ryu, Y.-H.,
690 Salamanca, F., Steeneveld, G. J., Tombrou, M., Voogt, J. A., Young, D. T., and Zhang, N.: Initial
691 results from Phase 2 of the international urban energy balance model comparison, International
692 Journal of Climatology, 31, 244-272, <https://doi.org/10.1002/joc.2227>, 2011.

693 Hang, J. and Chen, G.: Experimental study of urban microclimate on scaled street canyons with various
694 aspect ratios, Urban Climate, 46, 101299, <https://doi.org/10.1016/j.uclim.2022.101299>, 2022.

695 Hang, J., Zeng, L., Li, X., and Wang, D.: Evaluation of a single-layer urban energy balance model using
696 measured energy fluxes by scaled outdoor experiments in humid subtropical climate, Building and
697 Environment, 254, 111364, <https://doi.org/10.1016/j.buildenv.2024.111364>, 2024.

698 Hang, J., Lu, M., Ren, L., Dong, H., Zhao, Y., and Zhao, N.: Cooling performance of near-infrared and
699 traditional high-reflective coatings under various coating modes and building area densities in 3D
700 urban models: Scaled outdoor experiments, Sustainable Cities and Society, 121, 106200,
701 <https://doi.org/10.1016/j.scs.2025.106200>, 2025.

702 Hénon, A., Mestayer, P. G., Lagouarde, J.-P., and Voogt, J. A.: An urban neighborhood temperature and
703 energy study from the CAPITOUL experiment with the Solene model, Theoretical and Applied

704 Climatology, 110, 197-208, 10.1007/s00704-012-0616-z, 2012.

705 Imbert, C., Bhattacharjee, S., and Tencar, J.: Simulation of urban microclimate with SOLENE-
706 microclimat: an outdoor comfort case study, Proceedings of the Symposium on Simulation for
707 Architecture and Urban Design, Delft, Netherlands2018.

708 Kondo, A., Ueno, M., Kaga, A., and Yamaguchi, K.: The Influence Of Urban Canopy Configuration On
709 Urban Albedo, Boundary-Layer Meteorology, 100, 225-242, 10.1023/A:1019243326464, 2001.

710 Krayenhoff, E. S. and Voogt, J. A.: A microscale three-dimensional urban energy balance model for
711 studying surface temperatures, Boundary-Layer Meteorology, 123, 433-461, 10.1007/s10546-006-
712 9153-6, 2007.

713 Manoli, G., Faticchi, S., Schläpfer, M., Yu, K., Crowther, T. W., Meili, N., Burlando, P., Katul, G. G., and
714 Bou-Zeid, E.: Magnitude of urban heat islands largely explained by climate and population, Nature,
715 573, 55-60, 10.1038/s41586-019-1512-9, 2019.

716 Mei, S.-J. and Yuan, C.: Three-dimensional simulation of building thermal plumes merging in calm
717 conditions: Turbulence model evaluation and turbulence structure analysis, Building and
718 Environment, 203, 108097, <https://doi.org/10.1016/j.buildenv.2021.108097>, 2021.

719 Mei, S.-J., Chen, G., Wang, K., and Hang, J.: Parameterizing urban canopy radiation transfer using three-
720 dimensional urban morphological parameters, Urban Climate, 60, 102363,
721 <https://doi.org/10.1016/j.uclim.2025.102363>, 2025.

722 Nice, K.: Development, validation, and demonstration of the VTUF-3D v1. 0 urban micro-climate model
723 to support assessments of urban vegetation influences on human thermal comfort, School of Earth,
724 Atmosphere and Environment, Monash University, 2016.

725 Owens, S. O., Majumdar, D., Wilson, C. E., Bartholomew, P., and van Reeuwijk, M.: A conservative
726 immersed boundary method for the multi-physics urban large-eddy simulation model uDALES v2.0,
727 Geoscientific Model Development, 17, 6277-6300, 10.5194/gmd-17-6277-2024, 2024.

728 Reindl, D. T., Beckman, W. A., and Duffie, J. A.: Diffuse fraction correlations, Solar Energy, 45, 1-7,
729 [https://doi.org/10.1016/0038-092X\(90\)90060-P](https://doi.org/10.1016/0038-092X(90)90060-P), 1990.

730 Resler, J., Krc, P., Belda, M., Jurus, P., Benesova, N., Lopata, J., Vlcek, O., Damaskova, D., Eben, K.,
731 Derbek, P., Maronga, B., and Kanani-Suhring, F.: PALM-USM v1.0: A new urban surface model
732 integrated into the PALM large-eddy simulation model, Geoscientific Model Development, 10, 3635-
733 3659, 10.5194/gmd-10-3635-2017, 2017.

734 Rodriguez, A., Lecigne, B., Wood, S., Carmeliet, J., Kubilay, A., and Derome, D.: Optimal representation
735 of tree foliage for local urban climate modeling, Sustainable Cities and Society, 115, 105857,
736 <https://doi.org/10.1016/j.scs.2024.105857>, 2024.

737 Salim, M. H., Schlünzen, K. H., Grawe, D., Boettcher, M., Gierisch, A. M. U., and Fock, B. H.: The
738 microscale obstacle-resolving meteorological model MITRAS v2.0: model theory, Geoscientific
739 Model Development, 11, 3427-3445, 10.5194/gmd-11-3427-2018, 2018.

740 Schoetter, R., Caliot, C., Chung, T.-Y., Hogan, R. J., and Masson, V.: Quantification of Uncertainties of
741 Radiative Transfer Calculation in Urban Canopy Models, *Boundary-Layer Meteorology*, 189, 103-
742 138, 10.1007/s10546-023-00827-9, 2023.

743 Talebi, S., Gharehbash, K., and Jalali, H. R.: Study on random walk and its application to solution of heat
744 conduction equation by Monte Carlo method, *Progress in Nuclear Energy*, 96, 18-35,
745 <https://doi.org/10.1016/j.pnucene.2016.12.004>, 2017.

746 Toparlar, Y., Blocken, B., Vos, P., van Heijst, G. J. F., Janssen, W. D., van Hooff, T., Montazeri, H., and
747 Timmermans, H. J. P.: CFD simulation and validation of urban microclimate: A case study for
748 Bergpolder Zuid, Rotterdam, *Building and Environment*, 83, 79-90,
749 <https://doi.org/10.1016/j.buildenv.2014.08.004>, 2015.

750 Tregan, J. M., Amestoy, J. L., Bati, M., Bezian, J.-J., Blanco, S., Brunel, L., Caliot, C., Charon, J., Cornet,
751 J.-F., Coustet, C., d'Alençon, L., Dauchet, J., Dutour, S., Eibner, S., El Hafi, M., Eymet, V., Farges,
752 O., Forest, V., Fournier, R., Galtier, M., Gattepaille, V., Gautrais, J., He, Z., Hourdin, F., Ibarrart, L.,
753 Joly, J.-L., Lapeyre, P., Lavieille, P., Lecureux, M.-H., Lluc, J., Miscevic, M., Mourtaday, N.,
754 Nyffenegger-Péré, Y., Pelissier, L., Penazzi, L., Piaud, B., Rodrigues-Viguier, C., Roques, G., Roger,
755 M., Saez, T., Terrée, G., Villefranque, N., Vourc'h, T., and Yaacoub, D.: Coupling radiative,
756 conductive and convective heat-transfers in a single Monte Carlo algorithm: A general theoretical
757 framework for linear situations, *PLoS One*, 18, e0283681, 10.1371/journal.pone.0283681, 2023.

758 Tuholske, C., Caylor, K., Funk, C., Verdin, A., Sweeney, S., Grace, K., Peterson, P., and Evans, T.: Global
759 urban population exposure to extreme heat, *Proceedings of the National Academy of Sciences of the*
760 *United States of America*, 118, e2024792118, doi:10.1073/pnas.2024792118, 2021.

761 Villefranque, N., Hourdin, F., d'Alençon, L., Blanco, S., Boucher, O., Caliot, C., Coustet, C., Dauchet,
762 J., El Hafi, M., Eymet, V., Farges, O., Forest, V., Fournier, R., Gautrais, J., Masson, V., Piaud, B., and
763 Schoetter, R.: The “teapot in a city”: A paradigm shift in urban climate modeling, *Science Advances*,
764 8, eabp8934, doi:10.1126/sciadv.abp8934, 2022.

765 Voogt, J. A. and Oke, T. R.: Effects of urban surface geometry on remotely-sensed surface temperature,
766 *International Journal of Remote Sensing*, 19, 895-920, 10.1080/014311698215784, 1998.

767 Wang, K., Li, Y., Li, Y., and Lin, B.: Stone forest as a small-scale field model for the study of urban
768 climate, *International Journal of Climatology*, 38, 3723-3731, <https://doi.org/10.1002/joc.536>, 2018.

769 Wang, W., Wang, X., and Ng, E.: The coupled effect of mechanical and thermal conditions on pedestrian-
770 level ventilation in high-rise urban scenarios, *Building and Environment*, 191, 107586,
771 <https://doi.org/10.1016/j.buildenv.2021.107586>, 2021.

772 Wu, Z., Shi, Y., Ren, L., and Hang, J.: Scaled outdoor experiments to assess impacts of tree
773 evapotranspiration and shading on microclimates and energy fluxes in 2D street canyons, *Sustainable
774 Cities and Society*, 108, 105486, <https://doi.org/10.1016/j.scs.2024.105486>, 2024.

775 Yang, X. and Li, Y.: Development of a Three-Dimensional Urban Energy Model for Predicting and
776 Understanding Surface Temperature Distribution, *Boundary-Layer Meteorology*, 149, 303-321,
777 10.1007/s10546-013-9842-x, 2013.

778 Yang, X. and Li, Y.: The impact of building density and building height heterogeneity on average urban
779 albedo and street surface temperature, Building and Environment, 90, 146-156,
780 <https://doi.org/10.1016/j.buildenv.2015.03.037>, 2015.

781 Yoshida, K., Miwa, S., Yamaki, H., and Honda, H.: Analyzing the impact of CUDA versions on GPU
782 applications, Parallel Computing, 120, 103081, <https://doi.org/10.1016/j.parco.2024.103081>, 2024.

783 Yuan, C., Adelia, A. S., Mei, S., He, W., Li, X.-X., and Norford, L.: Mitigating intensity of urban heat
784 island by better understanding on urban morphology and anthropogenic heat dispersion, Building
785 and Environment, 176, 106876, <https://doi.org/10.1016/j.buildenv.2020.106876>, 2020.

786 Yuan, C., Shan, R., Zhang, Y., Li, X.-X., Yin, T., Hang, J., and Norford, L.: Multilayer urban canopy
787 modelling and mapping for traffic pollutant dispersion at high density urban areas, Science of The
788 Total Environment, 647, 255-267, <https://doi.org/10.1016/j.scitotenv.2018.07.409>, 2019.

789